RESEARCH ARTICLE

Impact of secondary particles on the magnetic field generated by a proton pencil beam: a finite-element analysis based on Geant4-DNA simulations

Martin Rädler[1] | **Giulia Buizza[2]** | **Maria Kawula[3]** |

Prasannakumar Palaniappan[1] | **Chiara Gianoli[1]** | **Guido Baroni[2]** |

Chiara Paganelli[2] | **Katia Parodi[1]** | **Marco Riboldi[1]**

[1]Department of Medical Physics, Faculty of Physics, Ludwig-Maximilians-Universität München, Munich, Germany

[2]Department of Electronics, Information and Bioengineering, Politecnico di Milano, Piazza Leonardo da Vinci, Milan, Italy

[3]Department of Radiation Oncology, LMU Hospital, Munich, Germany

Correspondence
Martin Rädler, Department of Medical Physics, Faculty of Physics, Ludwig-Maximilians-Universität München, Geschwister-Scholl-Platz 1, Munich D-80539, Germany.
Email: martin.raedler@physik.uni-muenchen.de

Abstract

Purpose: To investigate the static magnetic field generated by a proton pencil beam as a candidate for range verification by means of Monte Carlo simulations, thereby improving upon existing analytical calculations. We focus on the impact of statistical current fluctuations and secondary protons and electrons.

Methods: We considered a pulsed beam (10 μs pulse duration) during the duty cycle with a peak beam current of 0.2 μA and an initial energy of 100 MeV. We ran Geant4-DNA Monte Carlo simulations of a proton pencil beam in water and extracted independent particle phase spaces. We calculated longitudinal and radial current density of protons and electrons, serving as an input for a magnetic field estimation based on a finite element analysis in a cylindrical geometry. We made sure to allow for non-solenoidal current densities as is the case of a stopping proton beam.

Results: The rising proton charge density toward the range is not perturbed by energy straggling and only lowered through nuclear reactions by up to 15%, leading to an approximately constant longitudinal current. Their relative low density however (at most 0.37 protons/mm^3 for the 0.2 μA current and a beam cross-section of 2.5 mm), gives rise to considerable current density fluctuations. The radial proton current resulting from lateral scattering and being two orders of magnitude weaker than the longitudinal current is subject to even stronger fluctuations. Secondary electrons with energies above 10 eV, that far outnumber the primary protons, reduce the primary proton current by only 10% due to their largely isotropic flow. A small fraction of electrons (< 1%), undergoing head-on collisions, constitutes the relevant electron current. In the far-field, both contributions to the magnetic field strength (longitudinal and lateral) are independent of the beam spot size. We also find that the nuclear reaction-related losses cause a shift of 1.3 mm to the magnetic field profile relative to the actual range, which is further enlarged to 2.4 mm by the electron current (at a distance of $\rho = 50$ mm away from the central beam axis). For $\rho > 45$ mm, the shift increases linearly. While the current density variations cause significant magnetic field uncertainty close to the central beam axis with a relative standard deviation (RSD) close to 100%, they average out at a distance of 10 cm, where the RSD of the total magnetic field drops below 2%.

Conclusions: With the small influence of the secondary electrons together with the low RSD, our analysis encourages an experimental detection of the magnetic field through sensitive instrumentation, such as optical magnetometry or SQUIDs.

1 | INTRODUCTION

With several techniques currently under investigation, precise in vivo range verification for proton beam irradiation is a sought and critical step toward robust clinical ion-beam therapy.[1,2] The aim is to detect and compensate range shifts that originate from uncertainties in imaging, planning, patient setup, anatomical changes, etc. In addition to the existing approaches such as PET,[3] prompt gamma,[4] and ionoacoustics,[5] Albert et al.[6] proposed to detect the electric field of the primary protons. Subsequently, we further developed their analytical method to characterize the complete electromagnetic signal generated by a proton beam in different tissues.[7] Therein, it is shown that the rapid charge relaxation diminishes the electric field strength substantially due to the tissue's conductivity. In fact, collecting the associated charges through electrodes has recently been suggested as a dose monitoring system.[8] Eventually, we concluded the magnetic field, compared to the electric field, to be the favorable choice, which is approximately independent of the environment and directly correlated to the primary protons. Yet we already highlighted the shortcomings of the analytical approach, neglecting nuclear reactions, secondary protons and electrons, energy and range straggling, and lateral scattering.[7]

With the present work we seek to take these effects into account by means of Monte Carlo (MC) simulations. Some simplifying assumptions remain, which are discussed in Section 4.8. We also replace the analytical solution of the Maxwell equations with a numerical finite element analysis (FEA), which is one among numerous methods from computational electromagnetics.[9,10] Alternatives include integral methods based on Jefimenko's equations.[11] Compared to a previous approach,[12] we have simplified the FEA from a two-step process to a single calculation. We conduct an extensive analysis of the MC generated phase spaces (PS) together with a comparison of the associated charge and current density. From the latter, we estimate the magnetic field and analyze the impact of the hitherto neglected processes. With error propagation and the current density fluctuations extracted from MC, we also aim to quantify the magnitude of magnetic field uncertainties and gauge their impact on a measurement. Finally, we discuss a few aspects toward asMn experimental detection.

2 | METHODS

Throughout this work, many symbols, variables, and acronyms are used. For convenience, they are tabulated in the Supporting information (Section G).

2.1 | Finite element analysis

In the present work, we estimate the magnetic field from the MC data through the FEA. In particular, we apply a magnetostatic formulation due to the rapid response times (sub-nanosecond) of the magnetic field relative to the pulse duration[7]. The magnetic field strength quickly reaches its static value, only briefly deviated by an initial peak. Relaxation due to polarization effects are minute and also vanish in the nanosecond scale. Overall, the temporal profile of the magnetic field is quite simple, as it approximately follows the beam pulse shape. A similar beam pulse shape is also extracted from the ion source of the S2C2[13], an accelerator whose parameters guided the MC simulation settings (details in Section 2.3). Thus, we rather focus on the on average constant plateau value and calculate, by the use of the FEA, the spatial profile. For our application, the choice of FEA formalism requires careful consideration, as described in the following and further detailed in the Supporting information (Section A).

2.1.1 | Formulation

In the FEA, one utilizes the potential representation of the Maxwell equations, which are reformulated as a Lagrangian density. Minimizing the corresponding action solves the original differential equation according to the calculus of variations[14]. In the static case, we can neglect the dispersion. Assuming an isotropic and linear medium, the constitutive relations take the simple forms $\mathbf{D} = \varepsilon\mathbf{E}$ and $\mathbf{H} = \mathbf{B}/\mu$, where ε and μ are the static permittivity and permeability of the medium. Also, $\mathbf{E}$ and $\mathbf{B}$ are the electric field and magnetic flux density, while $\mathbf{D}$ and $\mathbf{H}$ are the electric displacement field and the magnetic field strength, respectively. Throughout this paper, we will refer to $\mathbf{B}$ just as the *magnetic field*, which is our primary quantity of interest. Upon the introduction of the scalar potential φ and the vector potential $\mathbf{A}$ as

$\mathbf{B} = \nabla \times \mathbf{A}$ and $\mathbf{E} = -\nabla\varphi - \partial\mathbf{A}/\partial t$, Ampère's circuital law takes the following form[15]:

$$\left(-\nabla^2 + \frac{1}{c^2}\frac{\partial^2}{\partial t^2}\right)\mathbf{A} + \nabla\left(\nabla \cdot \mathbf{A} + \frac{1}{c^2}\frac{\partial\varphi}{\partial t}\right) = \mu\mathbf{J}, \quad (1)$$

where $c = 1/\sqrt{\varepsilon\mu}$ is the speed of light in the medium and $\mathbf{J}$ is the free current density. The magnetostatic assumption $\partial\mathbf{A}/\partial t = 0$, is usually paired with the electrostatic assumption $\partial\varphi/\partial t = 0$, which with the identity $\nabla \times (\nabla \times \mathbf{A}) = \nabla(\nabla \cdot \mathbf{A}) - \nabla^2\mathbf{A}$, leads to the significantly simpler curl–curl equation[15–18]

$$\nabla \times \left(\frac{1}{\mu}\nabla \times \mathbf{A}\right) = \mathbf{J}. \quad (2)$$

Since the divergence of a curl vanishes by definition, Equation (2) implies that the input $\mathbf{J}$ has to be divergence-free (i.e., $\nabla \cdot \mathbf{J} = 0$). As we aim to calculate the magnetic field of a stopping pencil beam, where $\nabla \cdot \mathbf{J} \neq 0$, especially at the range, an approach based on Equation (2) is not suitable. The issue lies in the electrostatic assumption. Charges that are primarily deposited at the range, give rise to an electric field, that changes linearly in time for a beam with a constant current. Nonetheless, the charges do not accumulate at the range indefinitely. The conductivity of the target leads to charge relaxation with timescales ranging between a tenth and tens of nanoseconds, depending on the target tissue[7], which prohibits charge accumulation. Note that the associated charge transport is rather an exchange of electrons than an actual displacement of the primary protons. Also, the corresponding conductivity current density $\mathbf{J}_c = \sigma\mathbf{E}$, where σ is the conductivity, does not give rise to an additional magnetic field, due to the little charge transport that occurs during conduction and its flow along the radially symmetric $\mathbf{E}$. The latter follows directly from Maxwell's equations. Moreover, when it reaches the (discontinuous) boundary, $\mathbf{J}_c$ is distributed over a large volume and thus low compared to the compact and unidirectional beam current. The existence of external charges related to the proton's drift through air or the patient's skin has been ruled out by the measurements of Cirrone et al.[8]

Consequently, if $\nabla \cdot \mathbf{J} \neq 0$, then also $\partial\varphi/\partial t \neq 0$. Reintroducing the $\partial\varphi/\partial t$-term back into Equation (2) complicates the computations, however[12]. Nonetheless, the magnetic field estimation can be simplified considerably through the Lorentz gauge[15,17] $\nabla \cdot \mathbf{A} + \varepsilon\mu\partial\varphi/\partial t = 0$, whereby Equation (1), under the magnetostatic assumption, simplifies to the vector Poisson equation
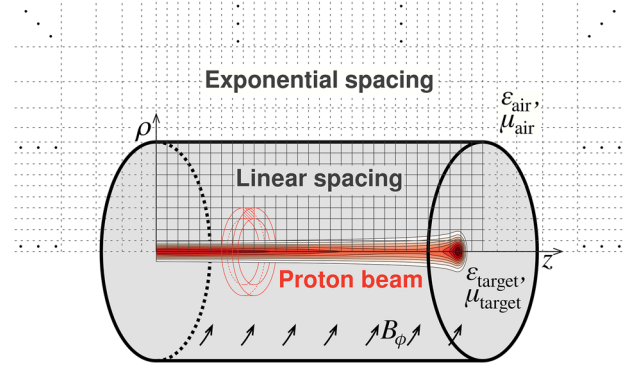
$$-\nabla^2\mathbf{A} = \mu\mathbf{J}, \quad (3)$$

FIGURE 1 Schematic sketch of the geometrical setup, current density tracking and magnetic field estimation. We took advantage of the cylindrical symmetry of a single proton pencil beam by collecting the 3D phase-space data into the 2D ρ–z-plane through square toroid shaped voxels (red volume). The nodes for the vector potential lie on the intersections of the grid lines, while the current density is defined on the pixels in between. The domain has been enlarged through exponential spacing, reaching far beyond the depicted area.

with the vector Laplacian on the left-hand side. Further analysis of Equation (3) is given in Section A.1.

2.1.2 | Magnetic field estimation

Through MC simulations (see Section 2.3 for details), we obtain multiple PS of a single proton pencil beam in water, where we take advantage of its cylindrical symmetry about the central beam axis. Thereby, the computations can be reduced to a 2D boundary value problem along the radius ρ and the beam axis z (see Figure 1). The following steps, outlined in the first two sentences of Section 2.1.1, are summarized in Section A.2.

For the minimization of the action, one discretizes and expands the vector potentials through nodal elements: $A_\kappa = \sum_i \tilde{A}_\kappa^i N_i(\rho, z)$, where $N_i(\rho, z)$ are the two-dimensional basis functions surrounding the nodal elements $\tilde{A}_\kappa^i$, which are arranged on a two-dimensional grid ($\kappa = \{\rho, z\}$). The accent $\tilde{o}$ shall separate physical quantities from nodal elements (with accent) expanding the physical quantities. Eventually, Equation (3) reduces to two separate systems of linear equations, summarized as

$$\underline{N}_\kappa \tilde{\mathcal{A}}_\kappa = \tilde{\mathcal{J}}_\kappa, \quad (4)$$

where the entries of the symmetric matrices $\underline{N}_\kappa$ describe the overlap of the basis functions. The vectors $\tilde{\mathcal{A}}_\kappa$ collect the nodal elements (i.e., $(\tilde{\mathcal{A}}_\kappa)_i = \tilde{A}_\kappa^i$), while $\tilde{\mathcal{J}}_\kappa$ contain the integrated current densities, weighted with the basis functions (i.e., $(\tilde{\mathcal{J}}_\kappa)_i = \tilde{J}_\kappa^i$). Explicit expressions are provided in Section A.3.

Finally, we obtain the magnetic field $\mathbf{B} = \nabla \times \mathbf{A}$ with $B_\phi = \partial A_\rho/\partial z - \partial A_z/\partial \rho$ through differentiation

$$B_\phi(\rho_i^B, z_j^B) = \sum_k \widetilde{A}_\rho^k \frac{\partial N_k(\rho_i^B, z_j^B)}{\partial z} - \sum_k \widetilde{A}_z^k \frac{\partial N_k(\rho_i^B, z_j^B)}{\partial \rho}$$

$$\equiv B_{\phi,\rho} \qquad\qquad + B_{\phi,z}, \qquad (5)$$

where we have defined a separation of the azimuthal magnetic field B_ϕ into the magnetic field that originates from radial current $B_{\phi,\rho}$ and the longitudinal current $B_{\phi,z}$.

Considering a detection outside of the target, that is, beyond the tissue's boundaries, we are effectively facing an unbound domain, namely the surrounding air. Furthermore, since the permeability of biological tissues, water and air are well approximated by the vacuum permeability ($\mu_r \approx 1$)[19], the domain is approximately homogeneous in the case of the static magnetic field.

For symmetry, we need to set the boundary at the central beam axis of $\widetilde{A}_\rho$ to zero. Instead of (arbitrarily) setting the remaining boundaries, we sufficiently enlarge the domain. To limit computational cost, we use exponentially increasing spacing as described in the subsequent section and shown in Figure 1. A broader discussion regarding the boundaries is provided in Section A.4.

2.1.3 | Domain discretization

Starting from the central beam axis, the radial vector potential grid is with $N_\rho^{lin} = 100$ samples initially linearly spaced, reaching up to $N_\rho^{lin}\Delta\rho = 10$ cm, where $\Delta\rho = 1$ mm. For the distance from 10 cm to 1 m, we used exponentially increasing spacing with $N_\rho^{exp} = 49$. The interval $[0, N_z^{lin}\Delta z]$ on the z-axis is with $N_z^{lin} = 150$ and $\Delta z = 1$ mm also linearly spaced. We set $z_0^A = 0$ to the depth where the beam enters the target, such that the range of 100 MeV protons in water is approximately in the center of the linear interval. Both the distal and proximal ends are similarly exponentially enlarged to approximately ± 1 m with $N_z^{exp} = 24$ samples each. Details have been summarized in the Supporting information (see Section A.5). The discrete ρ_i^A and z_i^A span a two-dimensional rectangular grid as illustrated in Figure 1. To put the exponential spacing into perspective, the linearly spaced area of interest (150×100 mm^2) constitutes merely 0.75% of the entire area, but is described by 51% of the sample points.

The midpoints between the grid lines ρ_i^J and z_i^J are the pixel centers of the discrete current density. For each pixel, we collected data from the associated square toroid volume (red ring in Figure 1), thereby taking advantage of the cylindrical symmetry. The kernels

at the outermost edges (i.e., at ρ_{max}^A, z_{min}^A, and z_{max}^A) require two pixels of ρ_i^J and z_i^J beyond, where we merely mirrored the preceding two pixels.

Finally, we interpolated the magnetic field with the differentiated interpolation kernels between the nodes at $\rho_i^B = (0.25 + i \times 0.5)$ mm for $i \in \{0, ..., 199\}$ and $z_i^B = (0.25 + i \times 0.5)$ mm for $i \in \{0, ..., 299\}$ on a square grid, thereby only evaluating the linearly spaced area.

2.1.4 | Numerical solution

With the domain specified above, $\underline{N}_\kappa$ are 29850×29850 matrices, where a numerical inversion is computationally feasible. For a discretized current density J_κ^i the entries of $\widetilde{\mathcal{J}}_\kappa$ from Equation (A7) are merely a weighted sum of J_κ^i, where the weights are the pixel-wise integrated interpolation kernels. Furthermore, the interpolation with the differentiated kernels from Equation (5) is also a weighted sum. Both can be represented by matrix multiplications: $\widetilde{\mathcal{J}}_\kappa = \underline{K}_J \mathbf{J}_\kappa$, $\mathbf{B}_{\phi,\kappa} = \underline{K}_\kappa \widetilde{\mathcal{A}}_\kappa$ and combined

$$\mathbf{B}_{\phi,\kappa} = \underbrace{\underline{K}_\kappa \underline{N}_\kappa^{-1} \underline{K}_J}_{\underline{M}_\kappa} \mathbf{J}_\kappa, \qquad (6)$$

where the vector $\mathbf{J}_\kappa$ collects the current density elements, calculated from MC. Therefore, the magnetic field $B_{\phi,\kappa}^i$ is yet a weighted sum of the discrete current density elements, with the weights collected in $\underline{M}_\kappa$. This representation is practical for an uncertainty and fluctuation estimation:

$$\sigma_{B_{\phi,\kappa}} = \left(\underline{M}_\kappa^{\circ 2} \sigma_{J_\kappa}^{\circ 2} \right)^{\circ 1/2}, \qquad (7)$$

where σ_{J_κ} and $\sigma_{B_{\phi,\kappa}}$ are the vectors containing the uncertainty of the current density and magnetic field and $\mathbf{v}^{\circ p}$ is the elementwise power as in $(\mathbf{v}^{\circ p})_i = v_i^p$.

2.2 | Current density accumulation

Let ρ_{max} mark the radial outer edge of the current, that is, $J_\kappa(\rho > \rho_{max}) = 0$. For an infinitely long and ϕ-symmetric current along z (i.e., $\mathbf{J} = J_z(\rho)\hat{\mathbf{e}}_z$), it follows directly from Ampère's circuital law that the azimuthal component of the magnetic field B_ϕ for $\rho > \rho_{max}$ depends only on the enclosed cross-sectional surface integral over $J_z(\rho)$ and drops off inversely proportional to the distance. In other words, since our primary interest is the field strength some centimeters away from the central beam axis, where $J_z = 0$, the exact shape of $J_z(\rho)$ does not affect the result and can thus be accumulated to a one-dimensional profile along z. This enables a simple evaluation of the impact of lateral scattering and

beam spot size in Section 3.2.2. In the following, we show how the accumulation rules emerge from the one-dimensional solutions along the radial axis. We will see below that they also apply in the two-dimensional case. We first recap the accumulation for J_z to facilitate the similar derivation for J_ρ.

2.2.1 | Accumulation for J_z

Setting $\partial^2 A_z/\partial z^2 = 0$ reduces Equation (A2) to one dimension. With $B_{\phi,z} \equiv -\partial A_z/\partial \rho$ and requiring $B_{\phi,z}(\rho \to 0) = 0$, one obtains the result by straightforward integration:

$$B_{\phi,z} = \frac{\mu}{\rho} \underbrace{\int_0^\rho \rho' J_z(\rho', z)d\rho'}_{\mathcal{I}_z(z)}. \tag{8}$$

The ρ'-weight is associated with the aforementioned surface integral in cylindrical coordinates. For $\rho > \rho_{max}$, the quantity $\mathcal{I}_z(z)$ is constant. As long as it equates to the same value, we can accumulate $J_z(\rho, z)$ to a one-dimensional profile. In particular, $\mathcal{I}_z(z_i^J) \approx \sum_j \widetilde{\rho}_j^J J_z(\rho_j^J, z_i^J)$, where $\widetilde{\rho}_i^J \equiv \int_{\rho_i^J-\Delta\rho/2}^{\rho_i^J+\Delta\rho/2} \rho' d\rho' = \rho_i^J \Delta\rho$. The accumulated current is then $J_z^{acc}(\rho_0^J, z_i^J) = \mathcal{I}_z(z_i^J)/\widetilde{\rho}_0^J$.

2.2.2 | Accumulation for J_ρ

Likewise, we simplify Equation (A1) with $\partial^2 A_\rho \partial z^2 = 0$. Setting the boundary conditions $A_\rho(\rho \to \{0, \infty\}) = 0$ leads to

$$A_\rho(\rho, z) = \frac{\mu\rho}{2} \int_\rho^\infty J_\rho(\rho', z)d\rho' + \frac{\mu}{2\rho} \underbrace{\int_0^\rho \rho'^2 J_\rho(\rho', z)d\rho'}_{\mathcal{I}_\rho(z)}. \tag{9}$$

The first term of $A_\rho(\rho, z)$ vanishes for $\rho > \rho_{max}$, while $\mathcal{I}_\rho(z)$ remains constant like $\mathcal{I}_z(z)$. Radial current further away from the central beam axis contributes for $\mathcal{I}_\rho(z)$ more due to the quadratic weighting as opposed to the purely geometrical linear weighting factor from $\mathcal{I}_z(z)$. The additional ρ-weight originates from the radial current flowing outward into larger volumes. Only a divergence-free and therefore source-free radial current $J_\rho \propto 1/\rho$ contributes equally like J_z. $J_\rho \propto 1/\rho$ implies current sources along ρ giving rise to stronger magnetic fields. In the present scenario, Coulomb scattering away or toward the central beam axis constitutes such sources. Accordingly, the radial accumulation differs and has been implemented as follows: $\mathcal{I}_\rho(z_i^J) \approx \sum_j \widetilde{\rho}_j^J J_\rho(\rho_j^J, z_i^J)$, where

$\widetilde{\rho}_i^J \equiv \int_{\rho_i^J-\Delta\rho/2}^{\rho_i^J+\Delta\rho/2} \rho'^2 d\rho' = (\rho_i^{J2} + \Delta\rho^2/12)\Delta\rho$ and therefore $J_\rho^{acc}(\rho_0^J, z_i^J) = \mathcal{I}_\rho(z_i^J)/\widetilde{\rho}_0^J$.

2.3 | Monte Carlo simulation

A volume of $41 \times 41 \times 103$ mm^3 was defined in Geant4 (version 10.5.p1)[20–22] to simulate interactions between an incident proton beam and a uniform material. Physical interactions were modeled using either the "option 5" constructor, made available through the Geant4-DNA extension[23–26] (abbreviated as DNA_5), or a standard physics list (QGSP_BIC) compatible with the processes from the constructor. In both cases, water was the chosen material.

For the present work, we consider a pulsed beam, as can be generated, for example, by a synchrocyclotron, over a continuous one, for example, from an isochronous[27]. Both can deliver maximum average currents in the order of tens/hundreds of nA's, which are required for standard clinical dose rates[28]. However, the pulsed operation creates stronger, albeit shorter, currents in the µA range, which give rise to larger magnetic field strengths. Analogous to the preceding analytical work[7], IBA's superconducting synchrocyclotron (S2C2)[29] serves here as a guideline regarding the choice of beam parameters. Its maximum average beam current and the pulse duration vary in the literature between $\sim 20-200$ nA[29–31] and $\sim 7-10$ µs[29,32,33] with a 1 kHz repetition rate. The maximum possible peak beam current of 18 µA is tabulated in[31]. For our simulations, we have chosen a more moderate peak beam current of $I = 0.2$ µA.

Particles were shot after sampling $x–y$-starting positions, from normal distributions. The beam current determines the average time delay between two consecutive protons: $\Delta t_p = q_e/I$, where q_e is the elementary charge. In our case: $\Delta t_p \approx 0.8$ ps. Since the differences of subsequent samples from any sorted uniform distribution can be well approximated by an exponential distribution, we introduce launch time fluctuations, by sampling Δt_p from $f_{\Delta t_p}(\delta > 0) = \exp[-\delta/\Delta t_p]/\Delta t_p$, leading to a random, but on average uniform current. By launching the protons with constant Δt_p instead, we observe that protons tend to occupy some z_i^J-bins more frequently, regardless of changing seeds. This implies that energy straggling shuffles the longitudinal position below the binning size Δz (more prominent for smaller z). A constant Δt_p is therefore not appropriate.

S2C2's uncertainty of the initial energy for a 230 MeV beam is 0.4 MeV, as given by Henrotin et al.[33] or Van de Walle[32]. Relative to the beam energy, this equates approximately to $\sigma_Q \approx 0.174\%$, which we applied to our chosen initial energy of $Q_{in} = 100$ MeV by sampling the initial energies from a normal distribution with $\mu_Q = Q_{in}$

and $\sigma_Q = 0.174$ MeV. For DNA_5, we used a spot size of $\sigma_b = 2.5$ mm, while we tested multiple spot sizes $\sigma_b = \{0.5, 1.0, \ldots, 5\}$ mm with QGSP_BIC, guided by Henrotin et al.[33] and Moteabbed et al[34].

We simulated independently (i.e., with different random seeds) the time from 0 to 0.9 ns, since, according to the continuous slowing down approximation (CSDA), it takes on average about $t_g \approx 0.81$ ns for the first protons to arrive at the range. We then exported the particle PS at randomly chosen times within $t_{PS} \in [0.85, 0.9]$ ns to describe the steady-state condition in a pulse. The t_{PS} variations target the same issue that motivated the random Δt_p sampling. We revert to the PS-based scoring, since current density, unlike dose, is not an accumulated quantity. Using multiple t_{PS} from the same simulation would lead to considerable and undesirable correlations and increased fluctuations. Also, different seeds allow a parallel implementation, which is necessary for the computationally expensive DNA_5 physics. The simulation time for one PS on a single CPU averages between 37–40 h. We deem $N_{PS} = 300$ PSs as sufficient statistics, revealing the weak and strongly fluctuating radial current.

The statistics allows an estimation of the current density standard deviation, which depends on the volume subdivision, that is, voxelization. Some technical remarks are given in Section B. We seek to estimate the standard deviation, since the actual particle count of moving protons in the target at any given time is comparatively low. Integrating Equation (D2) from Section D.1 across the target yields $\overline{n}_{tot} = \Phi(t_g - t_0) = I/q_e(t_g - t_0)$, which is merely the particle rate Φ multiplied with the average deceleration time $t_g - t_0$, where $t_0 = 0$ is the entrance time. With $I = 0.2$ μA, $\overline{n}_{tot} = 995$, while the count for the DNA_5 data is with $\overline{n}_{tot} = 962$ somewhat reduced due to nuclear reaction losses. For equal volume voxels (Section B) this means, there is an average of less than one proton per voxel. In other words, only very few protons give rise to the complete signal. The upper panel of Figure 2 shows a single PS sample, illustrating the low density.

2.3.1 | Extension of proton data

With Geant4, we only simulate the stopping of the beam in the target. Therefore, we need to add the preceding drift toward the entrance region, otherwise J_z would indicate a current source at $z = 0$, which changes the magnetic field profile. Assuming an initially normally distributed lateral beam profile with standard deviation σ_b and zero divergence drifting through vacuum, we simply have $\mathbf{J}(\rho, z < 0) = I/(2\pi\sigma_b^2) \exp[-\rho^2/(2\sigma_b^2)]\hat{\mathbf{e}}_z$. The proportion of the total beam current impinging on a cylindrical pixel element Ω within the radii $\rho_0 < \rho < \rho_1$ and the angular element $\phi_0 < \phi < \phi_0 + \Delta\phi$ is given by
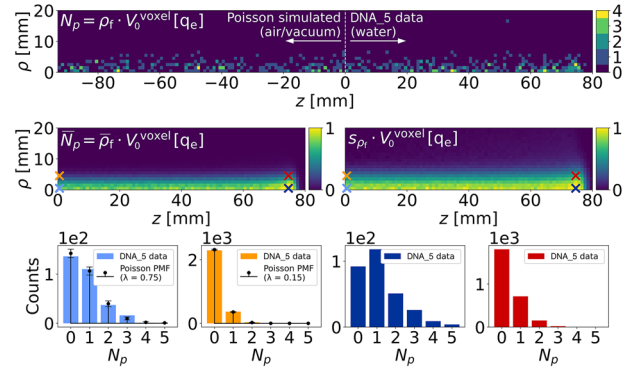

FIGURE 2 Beam extension based on Poisson distribution. The volume was subdivided into equal voxels V_0^{voxel} (see Section B). The upper panel for $z \geq 0$ shows a sample of a proton count distribution (i.e., charge in units of elementary charge q_e) from the DNA_5 data, hence the discretized colorbar. The data for $z < 0$ have been sampled from a Poisson distribution, with the mean given by Equation (11). For this demonstration, we kept $\Delta z = 1$ mm for $z < 0$, yet our actual geometry is exponentially spaced (Section 2.1.3 or Figure 1). The corresponding mean and standard deviation of the complete DNA_5 data are given below. In addition, we provided the underlying histograms at selected points, marked in the central row as crosses with the same color as the histogram bars. The two histograms at the entrance region, which are most similar to the free space drift, are further compared to Poisson probability mass functions (PMFs), with $\lambda = \overline{N}_p$, showing good agreement. The errorbars on the PMFs are the expected statistical deviations. For M samples, $\sigma_k^{PMF} = \sqrt{M p_k(1 - p_k)}$, that is, the standard deviation of a binomial distribution. For the equal volume subdivision, M changes with the radius. Therefore, the blue histograms add up to N_{PS}, while the red/orange ones, located at $\rho_4^J = 4.5$ mm, to $9 \times N_{PS}$.

$$I' = \iint_\Omega \mathbf{J} \cdot d\mathbf{A}$$

$$= \int_{\rho_0}^{\rho_1} \rho d\rho \int_{\phi_0}^{\phi_0+\Delta\phi} d\phi \frac{I}{2\pi\sigma_b^2} \exp\left(-\frac{\rho^2}{2\sigma_b^2}\right)$$

$$= I\left[\exp\left(-\frac{\rho_0^2}{2\sigma_b^2}\right) - \exp\left(-\frac{\rho_1^2}{2\sigma_b^2}\right)\right]\frac{\Delta\phi}{2\pi}. \quad (10)$$

From the partial current I', we can determine the average time delay between two adjacent protons $\Delta t_p' = q_e/I'$ and thus the average distance $\Delta z_p' = v_{in}\Delta t_p'$ through their initial velocity v_{in}. The latter in turn is determined by the initial kinetic energy: $v_{in}/c_0 = \sqrt{Q_{in}}\sqrt{Q_{in} + 2E_p}/(Q_{in} + E_p)$, where $E_p \approx 938.272$ MeV is the proton rest energy and c_0 is the speed of light. With the longitudinal grid spacing Δz, we can determine the average number of protons within each voxel:

$$\overline{N}_p = \Delta z/\Delta z_p' = I'\Delta z/(q_e v_{in}). \quad (11)$$

The actual proton count undergoes random fluctuations, which are well described by a Poisson distribution,

as shown in Figure 2, where the Poisson sampled data are even hardly distinguishable from the DNA_5 data.

Therefore, we complete the data by first sampling N_p from a Poisson distribution with $p_{N_p=k} = \lambda^k \exp(-\lambda)/k!$, with $\lambda = \overline{N}_p$. Subsequently, we draw N_p energy samples from a normal distribution with $\mu = Q_{in}$ and $\sigma = \sigma_Q$ and calculate their average velocity $\bar{v}$. Finally $J_z^{pre} = q_e N_p / V_i^{voxel} \bar{v}$, where V_i^{voxel} is the voxel volume from Section B. Likewise, we also extend the uncertainty through

$$\sigma_{J_z}^{pre} = q_e/V_i^{voxel} \sqrt{v_{in}^2 \sigma_{N_p}^2 + N_p \sigma_{v_{in}}^2}, \quad (12)$$

where the first term under the square root dominates due to the comparatively low $\sigma_{v_{in}}^2$ with respect to $\sigma_{N_p}^2 = N_p$ and for the second term we used the standard deviation of the mean $\sigma_{\bar{v}}^2 = \sigma_{v_{in}}^2/N_p$. In Figure B.1 (Supporting information), Equation (12) has been compared to the standard deviation in the entrance region of the DNA_5 data, confirming (i) the validity of Equation (12) and (ii) the applicability of the simple standard deviation on the DNA_5 data. Equation (12) also underlines the dependence of σ_{J_z} on the volume originating from σ_{N_p}, which is discussed in Section B. We do not need to extend the radial current J_ρ, assuming an initially divergence-free beam. Also, we assume that no secondary electrons are produced outside of the target due to the comparatively low density of the surrounding air.

2.3.2 | Range estimation from Monte Carlo generated phase spaces

We assign the peak of the diffluence (derivative of the fluence along the beam line) to the beam range, thereby applying the definition from Paganetti[35]. In particular, we calculate the current density $J_z(z_i)$ (with $z_i = (i + 1/2)\Delta z$ and $i \geq 0$) for stacked cylindrical volumes, that is, discs, perpendicular to the beam axis with $\Delta z = 0.25$ mm, and a radius r larger than the beam spot size. We then obtain the corresponding current by integration over the cross-sectional area: $I(z_i) = J_z(z_i)\pi r^2$. In order to compensate for the noise of the PS data, which is further enhanced through the required differentiation, we choose a smooth fit function. Based on Bohr's energy straggling theory[36], the distal fall-off can be described by an error function: $g(z|w_g, z_g, \sigma_g) \equiv g(z) = w_g/2\{1 + \text{erf}[-(z - z_g)/(\sqrt{2}\sigma_g)]\}$. The fit parameters w_g, z_g, and σ_g quantify the current strength prior to the drop, the range and the range straggling, respectively. Instead of excluding the data that corresponds to the preceding plateau, we continuously and smoothly attach a simple power law of the form $(az + b)^\alpha$, which models the decrease of fluence through nuclear reactions, in order to fit the

TABLE 1 Proton range for different Geant4 physics packages

Physics package	DNA_5	DNA_5 (Standard only)	QGSP_BIC
Range (mm)	76.31(4)	77.33(4)	77.72(4)

entire profile. In particular $f(z|w_g, z_g, \sigma_g, z_p, \alpha_p) \equiv f(z)$ with

$$f(z) = \begin{cases} g(z_p)\left(1 + \frac{g'(z_p)}{\alpha_p g(z_p)}(z - z_p)\right)^{\alpha_p} & z \leq z_p, \\ g(z) & z > z_p \end{cases} \quad (13)$$

where we join $g(z)$ and the power law at $z_p < z_g$. We find that the Geant4 physics package has a non-negligible impact on range, differing up to 1.4 mm (see Table 1). For reference, the NIST stopping power[37] combined with the CSDA predicts a range of 77.32 mm. Accordingly, we refrain from comparing data from different physics packages.

3 | RESULTS

Summarizing Section 2.3, we present results from two distinct simulations. First, the complex DNA_5 data, comprising 300 PSs of a pencil beam in water with a cross-section of 2.5 mm. Second, the simpler QGSP_BIC data with beam cross-sections ranging from 0.5 to 5.0 mm and otherwise identical parameters.

3.1 | Phase-space analysis

We begin with the analysis of the MC data, paying particular attention to velocity and charge density distributions of both protons and electrons to evaluate the current density from which the magnetic field is eventually calculated (Equation (6)). If not stated otherwise, we present the DNA_5 data. In the following, velocity-related quantities, that are given as percentages, are relative to the speed of light c_0. Also, $\kappa = \{\rho, \phi, z\}$ serves as a placeholder for the vector components in cylindrical coordinates.

3.1.1 | Protons

Statistical analysis.
The average proton velocities $\overline{v}_\kappa$ and their standard deviations s_{v_κ} are shown in Figure 4. All v_κ are well approximated by normal distributions, therefore $\overline{v}_\kappa$ and s_{v_κ} were determined through Gaussian fits. In terms of counts, magnitude and uncertainty v_κ vary significantly so that we adjusted the binning dynamically for each pixel. To ensure a balanced count per bin, we initially approximated mean μ and standard deviation σ with the
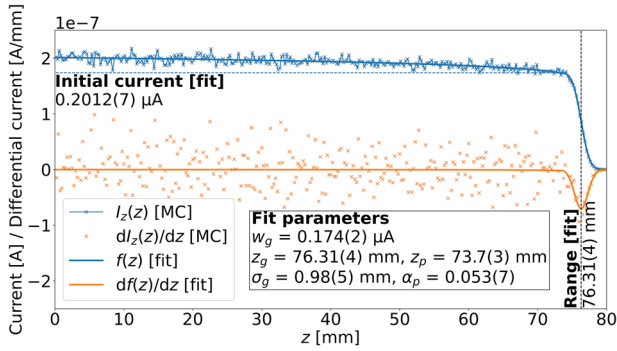
FIGURE 3 Current profile fit on the DNA_5 data with Equation (13) to determine the range. The values in parentheses are the 1σ uncertainties of the fit parameters, applying always to the last digits. The horizontal dashed line is the error function $g(z)$ (see the text above Equation (13)), technically only valid for $z > z_p$. It provides an estimate of the nuclear reaction related losses.
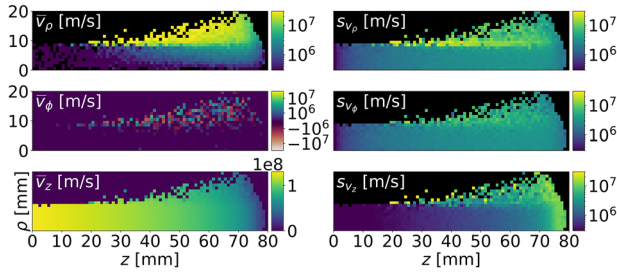

FIGURE 4 Average $\overline{v}_\kappa$ and standard deviation s_{v_κ} of the proton velocity along the components of a cylindrical coordinate system oriented along the beam axis. We collected data from all N_{PS} phase spaces (PSs), excluding pixels with less than 10 protons. Except for $\overline{v}_z$, the results are logarithmically scaled.

corresponding percentiles and set the histogram binning within $[\mu - 5\sigma, \mu + 5\sigma]$. This helps to compensate for outliers.

Beam distributions.
Some accumulated proton beam distributions are collected in Figure 5. The corresponding theoretical description is part of Section D.1. The complete dataset of N_{PS} PSs has been collected to enable a more statistically significant evaluation, while the results have been rescaled to represent the normalization of a single PS. Consequently, it is shown in the upper left panel of Figure 5 that a constant beam of 0.2 µA has a density of about 10 protons/mm in the entrance region, which increases to above 20 at the range.

Multiplying the charge density $q_e \tilde{f}_n^b(\mathbf{r})$ with the average velocity $\overline{v}_z(z)$ leads by definition to the current density, which is, upon lateral integration, the current $\tilde{I} = q_e \tilde{f}_n^b(z)\overline{v}_z(z)$. $\tilde{f}_n^b(z)$ is the already laterally integrated proton number density from Equation (D3). For $\overline{v}_z(z)$ in $\tilde{I}$, we used the linearly extrapolated velocity (dotted lines in Figure D.3) to avoid a sharp drop of $\tilde{I}$ at the range. $\tilde{I}$ is
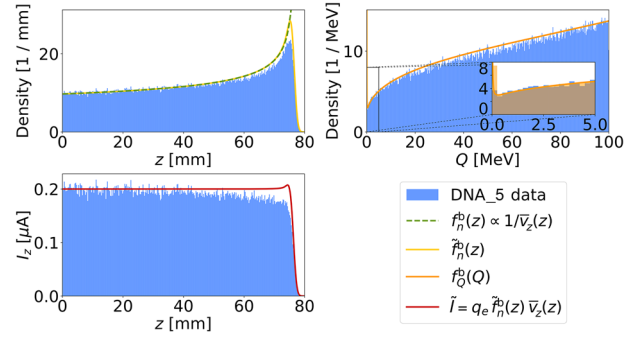

FIGURE 5 Summary of accumulated proton beam distributions during irradiation and considering only protons in motion. The theoretical expectations (dashed and solid lines) were derived in the Supporting information (Section D.1). $\tilde{f}_Q^b(Q)$ was additionally discretized (i.e., bin-wise integrated) in the inset of the upper right panel, due to the sharp peak close to $Q = 0$. The z-coordinates were binned with $\Delta z = 0.25$ mm, while the energies were binned with $\Delta Q = 0.25$ MeV.

in the lower left panel of Figure 5 compared to the MC data, which is essentially also shown in Figure 3.

3.1.2 | Electrons

The interaction cross-sections from DNA_5 are more accurate regarding the production of secondary electrons[23,25], than the standard QGSP_BIC physics list, especially for low energies. In fact, secondary, tertiary, etc., electrons with energies above 10 eV comprise about 92.3% of the exported PSs and thus far outnumber the primary protons. For QGSP_BIC they amount to about 0.02% only, while the primary protons constitute the vast majority. Yet, with 92.3%, there are on average only about 12 times more electrons than protons, while one might expect 4–5 orders of magnitude more. In particular, with an average secondary electron kinetic energy of 55 eV in water[38] and a mean ionization potential of 78 eV, we expect a total of 100 MeV/(78 + 55) eV $\approx 7.5 \times 10^5$ secondary electrons per primary proton. Significantly larger number of ionizations can also be found in the literature[39] with the theoretical descriptions through the interaction cross-sections discussed elsewhere[40–42]. Recall that DNA_5 tracks electrons down to 10 eV and does not use any production cuts for the DNA processes[24]. The apparent lack of electrons can be explained by their short lifetimes (sub-picoseconds) compared to the deceleration times of the primary protons (0.81 ns, as has been mentioned in Section 2.3). In fact, from our simulations, the average lifetime of the secondary electrons is just 7.5 fs, so when integrated over time, there are approximately 0.81 ns/7.5 fs $\approx 1.1 \times 10^5$ electrons in total. Given that despite the short lifetimes there are still 12 times more electrons than protons and taking the electrons with energies below 10 eV into account[38],
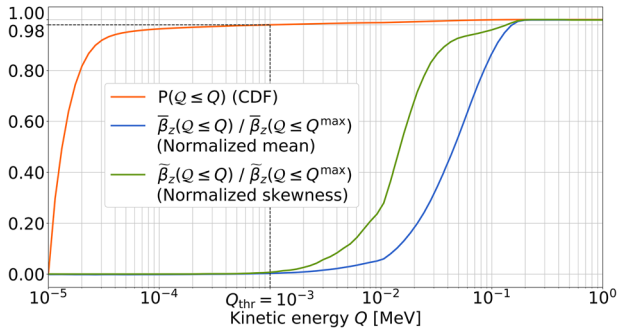
FIGURE 6 Normalized mean and skewness of the *z*-velocity from the complete secondary electron dataset as a function of increasing energies included, starting from $Q_{cut} = 10$ eV. Both the mean and the skewness (serving as a measure of symmetry) begin to deviate from a symmetric zero-mean distribution, only when electrons larger than our chosen threshold energy of $Q_{thr} = 1$ keV are included. These electrons amount to only 2% of the data, which follows from the cumulative distribution function (CDF): $P(Q \leq Q)$.
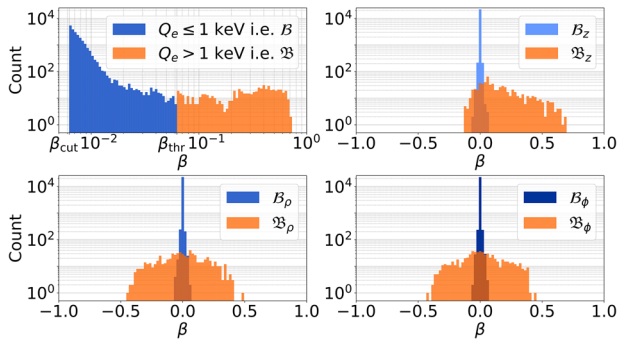

FIGURE 7 Logarithmic electron velocity distribution, relative to the speed of light, in the entrance region ($z_0 = 0.5$ mm, $\Delta z = 1$ mm, laterally integrated). Electrons are separated into low energies $\mathcal{B}$ (blue) and high energies $\mathfrak{B}$ (orange). The upper left panel, which shows the absolute velocity, is additionally logarithmic on the horizontal axis. The remaining panels are the velocity components in cylindrical coordinates.
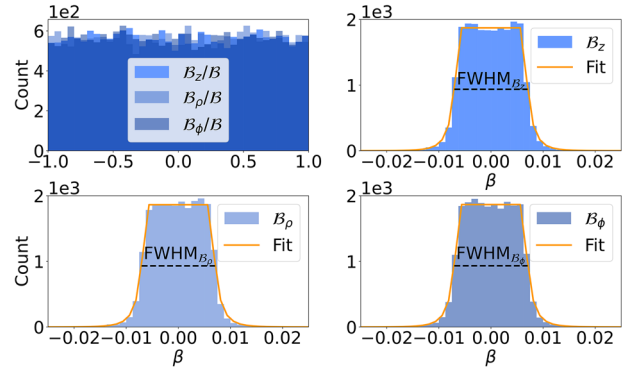

FIGURE 8 Low-energy electron velocity distributions, relative to the speed of light, in the entrance region ($z_0 = 0.5$ mm, $\Delta z = 1$ mm, laterally integrated). The upper left panel shows the distributions of the relative velocity components $\mathcal{B}_\kappa/\mathcal{B} \in [-1, 1]$, while the remaining panels are close-up histograms of $\mathcal{B}_\kappa \in [-\beta_{thr}, \beta_{thr}]$, also shown in Figure 7, here in a linear scale. The fit function for all $\mathcal{B}_\kappa$ is given by Equation (15).

there now seem to be many. Yet, the upper estimate refers to secondaries only, while Geant4-DNA simulates tertiary, etc., electrons. In summary, the factor of 12 refers to the *instantaneous* ratio between protons and electrons, not to an integrated one. In the following, we provide a statistical analysis of the electron distribution.

With respect to the velocity distribution, which is the primary focus here, we find that the secondary electrons can empirically be separated into two classes via the threshold energy $Q_{thr} = 1$ keV (see Figure 6), that is, threshold velocity $\beta_{thr} = 6.247 \times 10^{-2}$ (see Figure 7). Electrons with energies below the threshold show a narrow and isotropic distribution surrounding the primary protons, where their absolute velocity shall be denoted by $\mathcal{B}$ and the components by $\mathcal{B}_\kappa$. The vast majority, almost 98% of all electrons, belong to this class. Conversely, high energy electrons, with energies above Q_{thr},

follow a rather broad and anisotropic distribution (see Figure 7), represented by $\mathfrak{B}$ and $\mathfrak{B}_\kappa$.

Low-energy electron velocity distribution
The energy distribution is on the lower edge further thresholded by MC simulation related energy cuts set to $Q_{cut} = 10$ eV. Accordingly, the $\mathcal{B}$-distribution is also cut off at $\beta_{cut} \approx 6.256 \times 10^{-3}$, due to the monotone relationship between kinetic energy and velocity.

We seek to quantify the width of the $\mathcal{B}_\kappa$-distributions and thus analyze the impact of the energy cuts on $\mathcal{B}_\kappa$. The normalized velocity components are shown in the upper left panel of Figure 8, which are well described by uniform distributions, that is, $\mathcal{B}_\kappa/\mathcal{B} \sim \mathcal{U}_{[-1,1]}$. The present symmetry around zero indicates that the low-energy electrons flow indeed isotropically without a net drift across all $\mathcal{B}_\kappa$-components, as has been mentioned previously. By applying the latter in reverse, one obtains $\mathcal{B}_\kappa$ by multiplying $\mathcal{B}$ with samples from a uniform distribution. The resulting distribution as the product of the two random variables can be calculated through[43]

$$f_{\mathcal{B}_\kappa}(\beta) = \int_{-\infty}^{\infty} f_{\mathcal{B}}(\beta') f_{\mathcal{U}}(\beta/\beta')/|\beta'| d\beta'$$

$$= \frac{1}{2} \int_{|\beta|}^{\infty} f_{\mathcal{B}}(\beta')/\beta' d\beta', \qquad (14)$$

where we used that $f_{\mathcal{B}}(\beta < 0) = 0$. Based on the approximately linear decrease of $\mathcal{B}$ in the double-logarithmic histogram shown in Figure 7 (upper left panel), we describe $\mathcal{B}$ through a simple power law: $f_{\mathcal{B}}(\beta) \approx \alpha \beta_{cut}^\alpha/\beta^{\alpha+1}\theta(\beta - \beta_{cut})$ with the open parameter α. For simplicity, we tolerate the unphysical non-zero probability beyond 1, that is, $v > c_0$, which is, nevertheless, practically zero for the present parameter range. We

combine Equation (14) with the power-law distribution and obtain

$$f_{B_\kappa}(\beta) \approx \frac{\alpha}{2(\alpha+1)\beta_{cut}} \begin{cases} 1 & |\beta| \leq \beta_{cut} \\ (\beta_{cut}/|\beta|)^{\alpha+1} & |\beta| > \beta_{cut} \end{cases}. \quad (15)$$

The B_κ-distribution in Equation (15) is flat below the threshold velocity and, according to the same power law that applies to B, falls off symmetrically beyond β_{cut}. Based on the preceding empirical description, we choose the full width at half maximum (FWHM) of the B_κ-distribution as the desired measure for the distribution width (both Equation (15) and FWHM$_{B_\kappa}$ are shown in Figure 8):

$$\mathrm{FWHM}_{B_\kappa} = 2^{(\alpha+2)/(\alpha+1)}\beta_{cut}. \quad (16)$$

The standard deviation of B_κ is not suitable due to its truncated shape.

High-energy electron velocity distribution.
The high-energy secondary electron distributions (orange histograms in Figure 7) are significantly broader than the B_κ-distributions. While there is no drift along the radial ($\mathfrak{B}_\rho$) or azimuthal ($\mathfrak{B}_\phi$) direction, one can notice a shift of the $\mathfrak{B}_z$-distribution in the forward direction. In other words, these electrons tend to traverse downstream together with the primary protons. This directional current originates predominantly from single head-on electron proton interactions, known as hard collisions[44]. The maximum energy transfer is approximately given by $\Delta Q_{max} \approx 2\beta_p^2\gamma_p^2 E_e$, where $\beta_p = v_p/c_0$ is the primary proton velocity relative to the speed of light, $\gamma_p = 1/\sqrt{1-\beta_p^2}$, and E_e is the electron rest energy. Consequently, the maximum secondary electron velocity is well approximated by

$$\beta_e^{max} \approx 2\beta_p\gamma_p^2/(1+2\beta_p^2\gamma_p^2). \quad (17)$$

Longitudinal profile.
We extracted several statistical parameters from the depth-dependent electron distributions, such as the exemplary distributions in Figures 7 and 8 from the entrance region, and collected them in Figure 9. The electron data were laterally integrated within each z-bin, since the shape of the distribution does not change with the distance from the central axis, except for the decreasing statistics due to fewer primary protons. In other words, the almost isotropic electron cloud surrounding the primaries does not depend on the lateral position. In the following, we describe what is shown in Figure 9 from the bottom to the top.

The width of the low-energy velocity distribution is with FWHM$_{B_\kappa} \approx 1.41\%$ approximately constant along z. The percentage of high-energy electrons ($p_{Q_e > Q_{thr}}$) slightly decreases downstream due to the decreasing
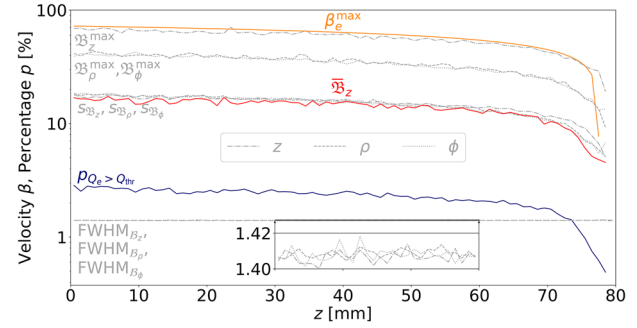
FIGURE 9 Statistical parameters from depth-dependent electron distributions extracted from N_{PS} DNA_5 phase spaces. FWHM$_{B_\kappa}$ is given in Equation (16), $p_{Q_e > Q_{thr}}$ is the percentage of electrons with kinetic energies above 1 keV, $\overline{\mathfrak{B}}_\kappa$, $s_{\mathfrak{B}_\kappa}$, and $\mathfrak{B}_\kappa^{max}$ are the mean, standard deviation, and maximum values of the $\mathfrak{B}_\kappa$-distributions (see Figure 7) and β_e^{max} is given in Equation (17).
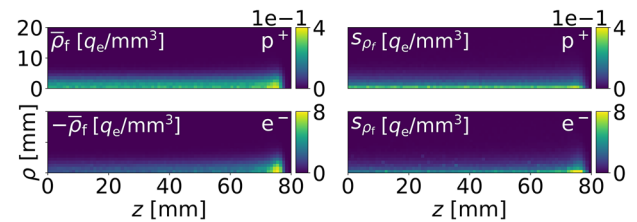
FIGURE 10 Charge density ρ_f of protons (p^+) and electrons (e^-). We show the mean of N_{PS} PSs on the left and the sample standard deviation on the right, which was estimated within increasing volumes (see Section B for details). We compensated the opposite charge of the electrons for clarity.

primary proton energy, starting from almost 3% in the entrance region down to below 1% at the range. The 2% estimate from Figure 6 is the average.

The high-energy standard deviations of the velocity ($s_{\mathfrak{B}_\kappa}$) as well as the mean velocity along z ($\overline{\mathfrak{B}}_z$) show an almost identical profile, gradually decreasing along z from about 17% down to 6%. The absolute maximum values $\mathfrak{B}_\rho^{max}$ and $\mathfrak{B}_\phi^{max}$ are shown as the 99.5th percentile, while $\mathfrak{B}_z^{max}$ is the 99.9th percentile. We have chosen the percentile over the overall maximum (100th percentile) since it follows the same trend, however it is interrupted by individual higher peaks that most likely originate from electrons involved in nuclear reactions. Finally, $\mathfrak{B}_z^{max}$ is compared to β_e^{max} from Equation (17), as a function of the depth-dependent primary proton velocity β_p.

3.2 | Charge and current density

3.2.1 | DNA_5 data

The charge density of a proton beam with $I = 0.2$ μA, together with its secondary electrons, is shown in Figure 10. The maximum proton density of
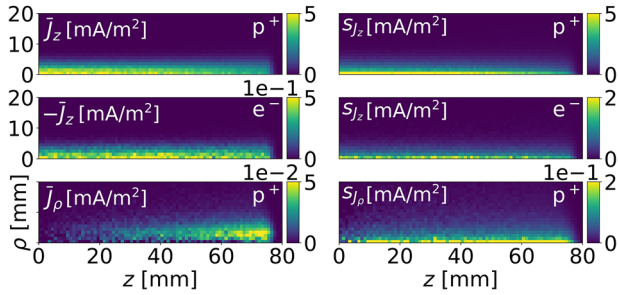
FIGURE 11 Current density of protons (p^+) and electrons (e^-) sorted by magnitude from strongest to weakest. See the caption of Figure 10 for further details.
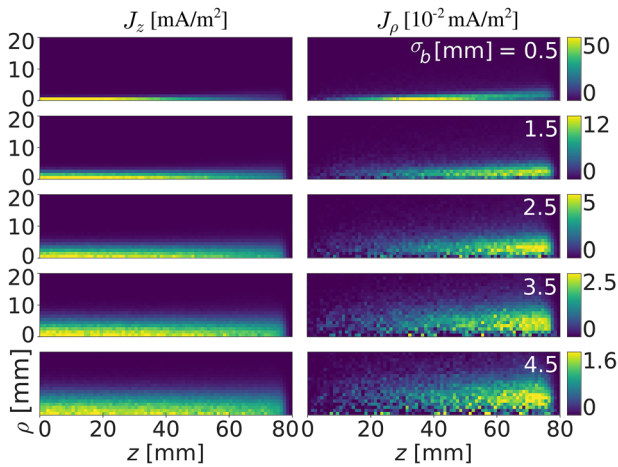

FIGURE 12 Simulated longitudinal (left) and lateral (right) proton current densities for increasing beam spot sizes $\sigma_b = \{0.5, \dots, 4.5\}$ mm. Only a subset of all σ_b is shown. The beam current is 0.2 μA for all spot sizes.

FIGURE 13 Accumulated longitudinal and radial current densities with different spot sizes from Figure 12 normalized to currents I_z and I_ρ through the gray areas. As opposed to Figure 12, all σ_b were included. The impact of scattering and thus the magnitude of I_ρ compared to I_z appears exaggerated, which is discussed in Section 4.4.

FIGURE 14 Radius-dependent range estimation for the DNA_5 data. For this purpose, we subdivided the data into annular rings (color-coded from small [blue] to large [red] radii) and determined the range based on error-function fits of the distal edge (right panel). The upper left panel shows the complete profiles, which, when added up, recover the profile from Figure 3 with 0.2 μA. The lower left panel collects the radius-dependent range values, compared to the overall range of 76.31 mm from Figure 3. The radially accumulated beam profile is shown on its right vertical axis.

approximately 0.37 p^+/mm^3, as mentioned in the abstract, is taken from the upper left panel. As previously mentioned, the numerous electrons with energies above 10 eV of the DNA_5 data far outnumber the primary protons by up to 20-fold, especially at the range. On the preceding plateau, the electron charge density is approximately 10 times larger. The average factor 12 follows from the overall statistics (see Section 3.1.2). The current density components of protons and electrons with non-zero average are summarized in Figure 11. For the calculation of the magnetic field with Equation (6), the data of Figure 11 have been used, where J_z of the protons needs to be expanded as described in Section 2.3.1.

3.2.2 | QGSP_BIC data with different spot sizes

In Figure 12, we have collected the average longitudinal and radial proton current density for different initial beam spot sizes, which have been simulated with
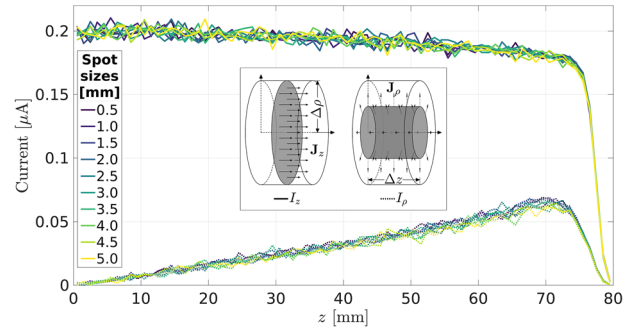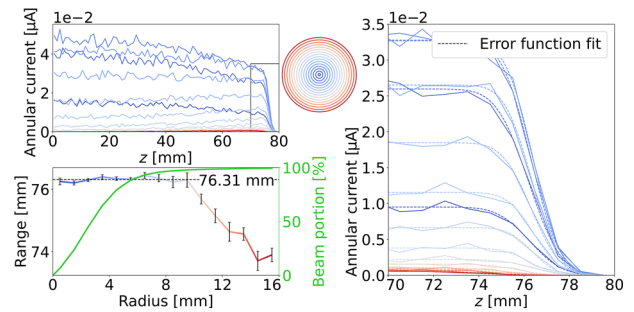
QGSP_BIC. We then applied the accumulation laws of Equations (8) and (9) for the one-dimensional comparison in Figure 13. The longitudinal current $I_z = J_z^{acc} \pi \Delta\rho^2$ is the flow through the circular cross-sectional area of the innermost disk. The radial current passes through a cylindrical area that changes within the pixel from zero to $2\pi\Delta\rho\Delta z$. We take the average, as depicted in Figure 13: $I_\rho = J_\rho^{acc} \pi \Delta\rho \Delta_z$.

For a more detailed analysis regarding the range, we show a radius-dependent range in Figure 14. This is motivated by the radially decreasing range as apparent in Figure 4 due to the longer proton paths from the lateral scattering.

3.3 | Magnetic field

Finally, we present the calculated magnetic field strengths, starting with Figure 15. Through Equation (5),
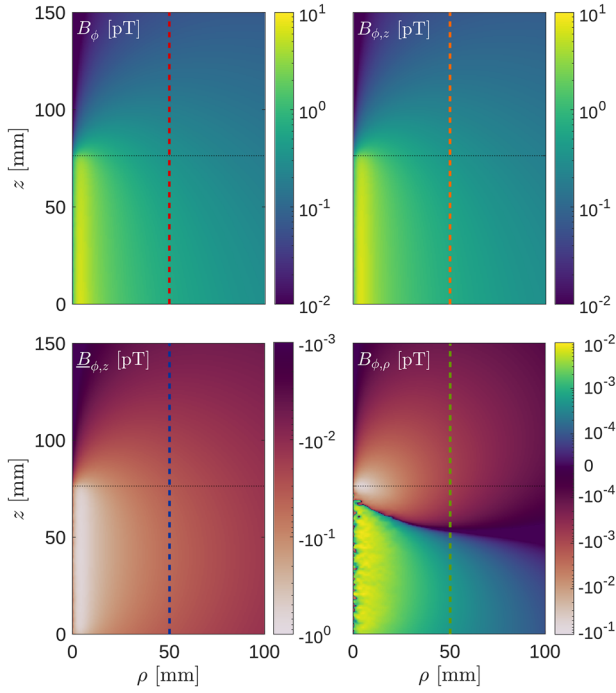
FIGURE 15 Magnetic field strength of a 0.2 μA beam from the average current densities of N_{PS} phase-spaces (PSs) (see Figure 11). The horizontal dotted lines indicate the range at 76.31 mm from Figure 3. The vertical dashed lines correspond to the profile plots from Figures 17 and 18, maintaining the same color code. The electron contribution is flipped due to the opposite charge.
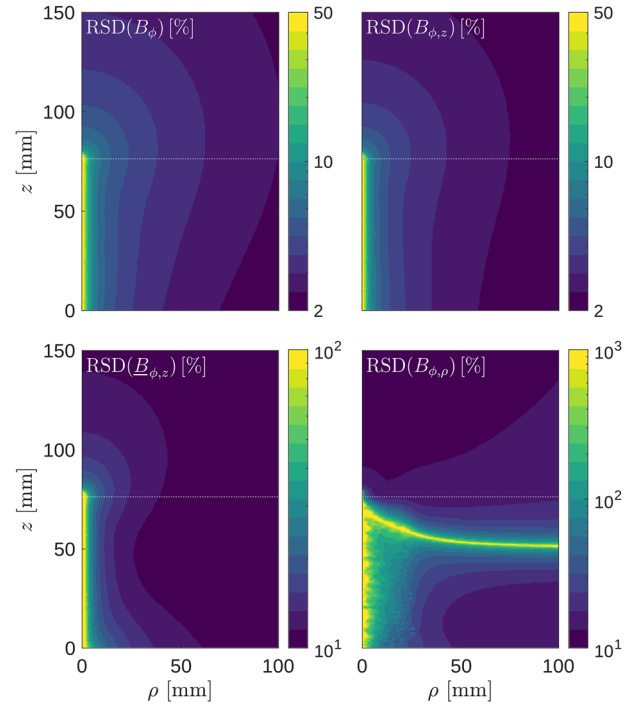

FIGURE 16 Relative standard deviation (RSD) of the results presented in Figure 15, with the current density uncertainty from the right column of Figure 11. See the caption of Figure 15 for further details.

the total azimuthal field B_ϕ has been separated into $B_{\phi,z}$ and $B_{\phi,\rho}$ that emerge from the z- and ρ-proton-currents and $\underline{B}_{\phi,z}$ from the electron current along z. With Equation (7), we calculated the uncertainties and represent the result in Figure 16 as absolute relative standard deviation, RSD $= \sigma/|\mu|$. The total uncertainty has been collected in the usual fashion: $\sigma^2_{B_\phi} = \sigma^2_{B_{\phi,z}} + \sigma^2_{\underline{B}_{\phi,z}} + \sigma^2_{B_{\phi,\rho}}$.

In Figure 17, we further analyze the magnetic field strength with profile plots parallel to the central beam axis at a distance of 5 cm. There, the results from Figure 15 are compared to the magnetic field strengths $B^{acc}_{\phi,z}$ and $B^{acc}_{\phi,\rho}$ from the accumulated currents J^{acc}_z and J^{acc}_ρ (see Sections 2.2.1 and 2). We estimated the uncertainty with Equation (7) and the standard deviation of the mean, that is, $\sigma_{J_\kappa} \to \sigma_{J_\kappa}/\sqrt{N_{PS}}$, which is not to be confused with the fluctuation estimation from Figure 16. In addition, we take the current profile from Figure 3 and calculate with the corresponding current density J^{fit}_z the magnetic field $B^{fit}_{\phi,z}$. Except for the noise, J^{fit}_z is identical to J^{acc}_z, hence the agreement between $B^{fit}_{\phi,z}$ and $B^{acc}_{\phi,z}$. The fit enables a further separation into the error-function current $J^{erf}_z = g(z)/(\pi\Delta\rho^2)$ and the attenuation-related current $J^{att}_z = [f(z) - g(z)]/(\pi\Delta\rho^2)$ (see Equation (13) and text above for details). Accordingly, $B^{fit}_{\phi,z} = B^{erf}_{\phi,z} + B^{att}_{\phi,z}$. Lastly, for reference we added the analytical result[7]
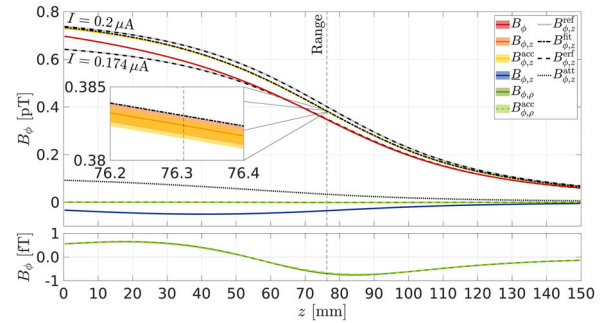
FIGURE 17 Magnetic field profiles along the vertical lines of Figure 15. $B^{acc}_{\phi,z}$ and $B^{acc}_{\phi,\rho}$ are the fields of the accumulated currents (Sections 2.2.1 and 2). We added the analytical result $B^{ref}_{\phi,z}$ from Equation (18) with the initial current of $I = 0.2$ μA and the error-function weight from Figure 3: $I = w_g = 0.174$ μA. The separation of the profile from Figure 3 into error-function and attenuation profile $B^{fit}_{\phi,z} = B^{erf}_{\phi,z} + B^{att}_{\phi,z}$ is also shown. The colored lines are surrounded by an error estimate, which is, however, due to its small size, only visible in the inset around the range. We also attached a closeup of $B_{\phi,\rho}$ and $B^{acc}_{\phi,\rho}$ on the bottom.

$$B^{ref}_{\phi,z} = \frac{\mu_0 I}{4\pi\rho}\left(1 - \frac{z - z_g}{\sqrt{\rho^2 + (z - z_g)^2}}\right) \quad (18)$$

which is obtained under simplified assumptions, that is, neglecting nuclear reactions and range straggling. The

FIGURE 18 Second derivative with respect to z of the results presented in Figure 17. See the caption of Figure 17 for a more detailed description.

apparent horizontal shift between $B_{\phi,z}^{\text{fit}}$ and the idealized $B_{\phi,z}^{\text{ref}}$ with $I = 0.2\ \mu\text{A}$ is further investigated in Figure 18. The second derivative of Equation (18) with respect to z has a root at the range:
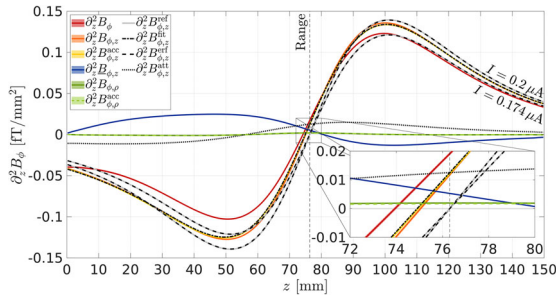
$$\frac{\partial^2 B_{\phi,z}^{\text{ref}}}{\partial z^2} = \frac{3\mu_0 I \rho}{4\pi} \frac{z - z_g}{\sqrt{\rho^2 + (z - z_g)^2}^5}. \qquad (19)$$

Hence, we estimate the second derivative of various results presented in Figure 17 as a simple approach to quantify range shifts with respect to the ideal $B_{\phi,z}^{\text{ref}}$. Analogous to Figure 17, the results have been collected in Figure 18. Computationally, we used the second-order central difference to approximate the differentiation.

4 | DISCUSSION

To summarize, we aimed to analyze the influence of secondaries (including nuclear reactions) and current density fluctuations on the magnetic field generated by a proton beam. We also investigated the impact of the beam spot size.

4.1 | Phase-space analysis: protons

We begin with the proton velocity analysis from Figure 4. Through scattering, the average radial velocity $\overline{v}_\rho$ increases downstream, while its standard deviation s_{v_ρ} remains approximately constant. The latter is for the most part larger than $\overline{v}_\rho$, leading to a relative uncertainty above 100%. Due to the cylindrical symmetry, we have $\overline{v}_\phi \approx 0$, with $s_{v_\phi} \approx s_{v_\rho}$, since both originate from Coulomb scattering. The positive and negative deviations from $\overline{v}_\phi \approx 0$ are related to low statistics. Finally, $\overline{v}_z$ dominates and is not exceeded by its uncertainty s_{v_z}, which increases longitudinally due to energy straggling. Yet, $s_{v_z}/\overline{v}_z < 1$ throughout. Overall, we expect the mag-

netic field from the radial proton current to be subject to larger fluctuations than from the longitudinal current.

The constancy of the beam current hinges upon the charge density increasing at the same rate as the velocity decreases. However, energy straggling and the corresponding penetration depth uncertainty has a distributing or spreading effect, potentially reducing the charge density. Hence, we analyze, whether the drop of current, as shown in Figure 3, can partially be attributed to energy straggling, which was the main purpose of the beam analysis presented in Figure 5. The expected main contributing process, reducing the beam current, are nonetheless the nuclear reactions, neglecting the weak lateral current (Figure 12). Comparing the more accurate $\tilde{f}_n^{\text{b}}(z)$, which includes energy straggling, with the ideal $f_n^{\text{b}}(z)$, we see that energy straggling has negligible impact prior to the range. Only the smooth drop of $\tilde{f}_n^{\text{b}}(z)$ at the range is caused by range straggling. Since we neglected the nuclear reactions during the calculation of $\tilde{f}_z^{\text{b}}(z)$ in Section D.1, the gradually increasing difference between $\tilde{f}_z^{\text{b}}(z)$ and the DNA_5 data can exclusively be attributed to nuclear reactions. Yet, the nuclear reactions do not eradicate the rise of the charge density along z, increasing to more than twice its initial value, which is a crucial characteristic that prevents a significant drop in magnetic field intensity. In fact, the difference between $\tilde{f}_n^{\text{b}}(z)$ and the DNA_5 data is at most 15%, which is also the ratio between the initial current and the weight w_g of the error function contribution from the fit of Figure 3. We can thereby largely confirm the expectation from a more analytical work[7], now on a MC basis.

Shortly before the range $\tilde{f}_n^{\text{b}}(z)$ even exceeds $f_n^{\text{b}}(z)$, since the spread of the sharp peak from $f_n^{\text{b}}(z)$ occurs longitudinally in both directions. Upon close inspection, this is visible in the upper left panel of Figure 5, but much more pronounced for $\tilde{I}$ in the lower left. Note that the velocity extrapolation, used in $\overline{v}_z(z)$, provides an accurate description of the data.

Finally, the DNA_5 energy distribution is well described through the idealized $f_Q^{\text{b}}(Q)$, given that a symmetric blurring has little impact. Based on the increasing number density distribution along z and that the average proton energy decreases downstream, the naïve expectation of the energy distribution would be that it rises toward lower energies. Yet, both the theoretical description $f_Q^{\text{b}}(Q)$ and the DNA_5 data exhibit a contradicting distribution. The explanation of this counterintuitive result lies within the concave shape of $z(Q)$, that originates from the increasingly more rapid energy-loss downstream. Therefore, an energy interval ΔQ is initially associated with a wide Δz, which decreases with lower energies. Accordingly, the distribution should have more particles with higher energies and fewer with low energies. The opposing expectation, based on the shape of $\tilde{f}_n^{\text{b}}(z)$, is therefore not invalid but merely overshadowed by the countering $z(Q)$-effect. In fact, the

former effect dominates for very low energies, where the curvature of $z(Q)$ changes, leading to a minimum of $f_Q^b(Q)$ close to $Q = 0$ (see the inset of the upper right panel of Figure 5).

4.2 | Phase-space analysis: electrons

The empirical sub-division at $Q_{thr} = 1$ keV is well justified with Figure 6, enabling a simple separation into relevant high-energy and negligible low-energy electrons. The directionality of the secondary electrons is dictated by the *binary encounter peak angle*[45]. For track-structure codes, such as Geant4-DNA, it is applied for energies above 100 eV[46,47]. In our results (see Figure 6), we can only see very slight forward scattering above 100 eV, since the deflection angle is almost perpendicular to the primary proton track for such low energies. A practical conclusion for future work is to raise the cut energy to the threshold energy, which should accelerate simulation times significantly, since only 2% of the DNA_5 data need to be simulated and saved to obtain the same results.

In Section 2.1.1, we have argued that the homogeneous charge relaxation current does not lead to an additional magnetic field, yet it has not been discussed whether the secondary electrons increase the conductivity, which would lead to an asymmetric current. We would argue that the latter is not the case, for the following two reasons. First, while there are 10^5–10^6 electrons per primary proton, their density remains low relative to the ionic charge carriers of the target, which is in the order of Avogadro's number. Recall that the primary protons have low densities themselves (see Figure 2). The second reason are the immensely short lifetimes of secondaries. As mentioned in Section 3.1.2, they are sub-picoseconds with energies above 10 eV and captured quickly thereafter. Alternatively, they enter a *solvated* state within the same timescales that lies below the conduction band[48]. This means that while the primary proton is still underway, its secondary electrons are already absorbed. Simultaneously, the charge relaxation times are above the nanosecond scale[7], so that the primary protons downstream cannot exert a drift on the short-lived electrons.

The symmetric low-energy electron distributions are shown in Figure 8. It follows straight from Equation (14) that any $\mathcal{B}$-distribution with a lower threshold will lead to a plateau within $|\beta| \leq \beta_{cut}$ for $\mathcal{B}_\kappa$ as long as $\mathcal{B}_\kappa/\mathcal{B} \sim \mathcal{U}_{[-1,1]}$. This provides an explanation for the unexpected plateau in $\mathcal{B}_\kappa$ as a mere consequence of the MC cut energy. The empirical power-law fit provided a close description of the $\mathcal{B}_\kappa$-distributions, yet it fails to capture the tails. With the sharp drop of the power-law ($\alpha_\kappa \approx$ 4.89(2)) $f_{\mathcal{B}_\kappa}(\beta)$ is hardly broader than the cut velocity such that $\mathrm{FWHM}_{\mathcal{B}_\kappa} \approx 2\beta_{cut}$. Hence, a somewhat higher Q_{cut} would have eradicated the vast majority of elec-

trons, as can also be confirmed with Figure 6. Compared to the target electrons, the instantaneous density of secondary electrons remains comparatively low so that together with their short lifetimes, high velocities (10 eV corresponds to 0.6% of c) and random trajectories, one can neglect their mutual interactions. In hindsight, this also justifies the use of MC.

From Figure 7, we see that the small shift of $\mathfrak{B}_z$ toward positive velocities gives rise to the complete electron current. Note that even though the primary protons do exhibit a radial drift, the same cannot be observed for the secondary electrons. The comparatively low strength and the strong fluctuations of the primary proton velocity (Figure 4) suppress a radial trend of the electron flow.

The summary of Figure 9 shows that the homogeneous electron cloud is constant along the beam. This allows for a collective analysis of the low-energy electrons, integrated also along z. Instead of the power law, it is probably more natural to consider a normal distribution for the velocity components $\mathcal{B}_\kappa$. Some theoretical considerations and the corresponding truncated normal distribution are given in Section C together with the fit in Figure C.2. While the Gaussian model demonstrates a good description of the data in the linear scale and close to β_{cut}, large discrepancies emerge in the logarithmic scale, with the data included up to β_{thr}. Yet, the Gaussian model is worthwhile, since it allows an extrapolation and furthermore an estimate of the total number of electrons if no energy cuts were applied, that is, $Q_{cut} = 0$. By this approach, there should be 4.7 ± 0.2 times more low-energy electrons. Accordingly, the high-energy fraction shrinks from 2% (from Figure 6) to below 0.5%. However, this analysis is deliberately not part of the results, being a somewhat crude extrapolation based on comparatively little truncated data.

The non-zero longitudinal electron drift $\overline{\mathfrak{B}}_z$ (red line of Figure 9) is strongly perturbed by the uncertainties $s_{\mathcal{B}_\kappa}$ of almost identical magnitude, which can already be appreciated in Figure 7. With the corresponding relative uncertainty close to one, just like v_ρ of the protons, we also expect larger magnetic field uncertainties. Finally, the upper threshold of the $\mathfrak{B}_z$-distribution $\mathfrak{B}_z^{max}$ is well described by the depth-dependent maximum energy of the secondary electrons β_e^{max} from Equation (17) (orange line of Figure 9). This supports the statement from above that the $\mathfrak{B}_\kappa$-electrons result from hard, that is, head-on, collisions. These interactions solely give rise to the relevant electron current.

4.3 | Charge and current density

The longitudinally increasing proton charge density is indeed also present in Figure 10. Likewise its uncertainty s_{ρ_f} increases, indicating that the initial Poissonian uncertainty also applies downstream, which increases

with the square root of the proton counts. The magnitude of s_{ρ_f} is comparable to $\bar{\rho}_f$ itself due to the low proton counts per voxel. Yet again, Figure 10 shows the abundance of electrons over protons. However, the larger electron counts also undergo uncertainties of comparable size, much like the protons, despite the larger statistics. Therefore, the Poissonian expectation does not apply to the electrons. The latter can be explained bearing in mind that the secondary electrons do not scatter far away from the primary protons. If a proton occupies a voxel, then so do many secondary electrons. Similarly, the absence of protons leads to an absence of electrons (*"all-or-nothing"*). This close correlation lets the electron counts fluctuate like the protons, just in larger quantities.

The proton current strength $\bar{J}_z$ in Figure 11 decreases longitudinally due to lateral scattering and nuclear reaction related losses. The increasing s_{ρ_f} is suppressed in s_{J_z} due to the decreasing velocity ($\bar{J}_z = \bar{\rho}_f \bar{v}_z$). Moreover, the impact of the rising v_z-fluctuations (Figure 4), as a result from energy straggling, is comparatively low and can therefore not be observed in s_{J_z}. In terms of strength, the electron current is approximately one order of magnitude weaker than the proton current. Yet, there are approximately 10 times more electrons with energies above 10 eV than protons (certainly more, considering Figure C.2). This discrepancy is resolved with the foregoing PS analysis of the electrons. We had that only 2% of electrons contribute to the non-zero average, which compensates the two orders of magnitude difference. These electrons ($\overline{\mathfrak{B}}_z$ from Figure 9) are on average slower than the protons, whose velocity is comparable to $\mathfrak{B}_\rho^{max}$ or $\mathfrak{B}_\phi^{max}$. Their maximum speeds up to $0.7 \times c_0$ contribute to the large variability, which is also explained by the low relevant electron counts. In summary, few swift electrons comprise the electron current, as opposed to many slow ones. Yet another order of magnitude weaker is the radial proton current, with an relative uncertainty below one. Its contribution to the magnetic field will be negligible.

4.4 | Spot size impact

For small beam spot sizes (0.5–2.5 mm), the lateral scattering leads to an apparent drop in longitudinal current density J_z, as can be seen on the left panel in Figure 12. However, while the field strength close to the central beam axis might be impacted, the accumulated currents I_z from Figure 13 are equal, implying no field strength differences among different spot sizes in the far-field. This is a rather expected behavior based on Ampère's law, since the current for, for example, $\sigma_b = 0.5$ mm and $z > 40$ mm is more spread out but still flows approximately in parallel. For larger spot sizes, this effect is less pronounced, due to an approximate equilibrium of scattering toward and away from the central beam axis.

The radial scattering increases downstream, except for $\sigma_b = 0.5$ mm, which is dominated by the aforementioned increasing spreading. Comparing the current strengths of J_z to J_ρ for each σ_b (left vs. right in Figure 12), J_ρ is once again approximately two orders of magnitude weaker than J_z. Yet, the accumulated radial currents I_ρ in Figure 13 are comparable to I_z, whereby similar field strengths could be expected. However, while $B_{\phi,z} \propto J_z$, $B_{\phi,\rho} \propto \partial J_\rho/\partial z$, depending on the change of J_ρ along z. Therefore, it is not sensible to compare I_z and I_ρ regarding the corresponding field strengths. It is unexpected, however, that also J_ρ, under the square weight accumulation of Equation (9), integrates to a spot size independent profile (see Figure 13). Nonetheless, we find that this result is indeed supported by simple scattering theory (Fermi–Eyges). Details are given in the Supporting information: Section E. Altogether, neither J_z nor J_ρ are affected by the spot size in the far-field. This also holds true for beam spot sizes larger than the simulated 5 mm.

4.5 | Two-dimensional magnetic field profiles

The total azimuthal magnetic field B_ϕ is dominated by the longitudinal current J_z and only slightly lowered by the electron current (Figure 15). The impact of the radial current is negligible. Since $B_{\phi,\rho} \propto \partial J_\rho/\partial z$, as mentioned previously, its strongest contribution is at the range due to the sharp drop of current. It changes sign, since the radial current initially increases (as shown in Figure 13). Since we did not extend the radial and electron current, we see that $B_{\phi,\rho}$ and $\underline{B}_{\phi,z}$ approach zero toward $z = 0$, as opposed to $B_{\phi,z}$.

The separation into individual PSs enabled an estimation of uncertainty, which we translated to the B_ϕ uncertainty through Equation (7). To clarify the interpretation of the results in Figure 16, they quantify, more specifically, the variability of the resulting magnetic field from different *static* PSs. The dynamic nature of the process is neglected, in particular the propagation of the field to the detector, which strongly depends on the medium[7]. Nonetheless, Figure 16 confirms the overall expectation, that the strong current density fluctuations (Figure 10) lead to high RSD. The further we move away from the central beam axis, the more current elements contribute to the signal, averaging out the fluctuations. The zero-crossing of $B_{\phi,\rho}$ causes the high RSD around $z = 50$ mm. Overall, the magnitude of the RSDs is in line with the s_{J_x} from Figure 10, with the dominant contribution once again from the longitudinal proton current. The results from Figure 16 focus on the azimuthal component. The v_ϕ uncertainties (Figures 4 and 9) lead to

B_ρ and B_z fluctuations, which are likely of similar magnitude, but cannot be estimated under our symmetry assumptions from Section 2.1.2. Due to the rapid proton velocities (Figure 4), the fluctuations should be in the nanosecond time scale, that is, in the GHz frequency range. They are not expected to disturb a measurement means of optical magnetometry, which is further discussed in Section F.

4.6 │ One-dimensional magnetic field profiles

First and foremost, Figure 17 confirms the accumulation rules from Sections 2.2.1 and 2 due to the excellent agreement between $B_{\phi,\kappa}$ and $B_{\phi,\kappa}^{\mathrm{acc}}$. Also, the analytical references $B_{\phi,z}^{\mathrm{ref}}$ from Equation (18) with the initial current of $I = 0.2$ μA and the remaining range current of $I = 0.174$ μA are indistinguishable from $B_{\phi,z}^{\mathrm{erf}}$, which are based on smoother current profiles as opposed to the sharp step used for Equation (18). Hence, range straggling does not perturb or shift the magnetic field profile in the far-field. In addition, the two $B_{\phi,z}^{\mathrm{ref}}$ provide an envelope for the more accurate $B_{\phi,z}$, which is as expected, since J_z transitions continuously from 0.2 to 0.174 μA (Figure 3). Yet, it appears shifted back with respect to the 0.2 μA profile. A natural explanation might be the lateral scattering leading to shorter projected ranges due to the curved paths. This effect is, for example, present in Figure 4. We inspected this hypothesis with Figure 14. While the range is indeed longitudinally shifted for larger radii, the vast majority of protons maintain the range close to 76.31 mm. The scattering does not provide an explanation for the shift. Therefore, in Figure 17 we separately show the $B_{\phi,z}$-field contribution related to the attenuation $B_{\phi,z}^{\mathrm{att}}$.

The zero-crossing of the second derivative provides a simple assessment of a $B_{\phi,z}^{\mathrm{att}}$ related profile shift (Figure 18). This criterion has been chosen, since it is less susceptible to differences in magnitude, that is, $B_{\phi,z}^{\mathrm{ref}}(I = 0.174$ μA) may appear shifted horizontally with respect to $B_{\phi,z}^{\mathrm{ref}}(I = 0.2$ μA) in Figure 17, but both $\partial_z^2 B_{\phi,z}^{\mathrm{ref}}$ pass through zero precisely at $z_g = 76.31$ mm in Figure 18. And indeed, with $\partial_z^2 B_{\phi,z}^{\mathrm{att}} > 0$ at the range, $\partial_z^2 B_{\phi,z}$, $\partial_z^2 B_{\phi,z}^{\mathrm{acc}}$ and $\partial_z^2 B_{\phi,z}^{\mathrm{fit}}$ are equally shifted back by approximately 1.3 mm. Electrons together with the radial current further enlarge the distance from z_g and the zero-crossing of B_ϕ to roughly 2.4 mm. Note that the shift changes with the radius. For $\rho > 45$ mm, it increases linearly and can thus be described by $z[\mathrm{mm}] = p_1 \cdot \rho[\mathrm{mm}] + p_0$, where $p_1 = -0.0709(1)$ and $p_0 = 77.47(1)$ mm. In summary and ordered from most to least contributing, the shift originates from the atten-

uation of nuclear reactions, the electron current and the radial proton current.

In terms of magnitude, $B_{\phi,z}^{\mathrm{att}}$ approximately cancels $\underline{B}_{\phi,z}$, which is why B_ϕ is well approximated by $B_{\phi,z}^{\mathrm{ref}}(I = 0.174$ μA). Just as in Figure 15, since both the electron and radial proton current only exist inside the target, $\underline{B}_{\phi,z}$ and $B_{\phi,\rho}$ trend toward zero for $z < 0$.

4.7 │ Toward detection

Having presented a detailed analysis of the magnetic field that originates from a proton pencil beam, we can now roughly evaluate a potential clinical applicability. The underlying principle is that the longitudinal profile carries information about the range. We have shown that technically it could be extracted from the second derivative with respect to z, where attenuation, electron current and radial proton current related shifts need to be compensated. Yet, the necessary sensitivity to probe second-order variations of the B-field directly seems beyond current technical capabilities. For our work, we have used $\partial_z^2 B_\phi$ as a tool to quantify the impact of effects that have been neglected thus far. A more direct approach would be to measure the magnetic field itself. One could then obtain the range by optimizing the agreement between the measured and expected profile of B_ϕ along z as it is shown in Figure 17. As its range is known, it could be inferred from the measured data.

In terms of magnitude, this seems feasible. In particular, assuming a sensitivity of 3.6 fT/$\sqrt{\mathrm{Hz}}$[49] and a pulse duration of 10 μs one may detect field strengths of 1 pT. For our calculations, we have considered rather small beam spot sizes (2.5 mm) and currents that lie well within the technical limitations of S2C2 so that the dose of a single pulse is comparatively low: 37 mGy. Considering a more practical spot size of 7.5 mm (relying on spot size independence, as investigated with Figure 13) and allowing for a dose of 0.1 Gy, the peak beam current can be about 20 times larger, while S2C2 can deliver up to 100 times larger peak beam currents[31] and somewhat longer pulses[13]. Accordingly, the field strength rises from about 0.5 (Figure 17) to 10 pT, one order of magnitude above the sensitivity limits. A further enhancement can be achieved by averaging the signal over multiple pulses, as has been done in the work of Lehrack et al.[50], investigating ionoacoustics as an alternative range verification approach.

Higher doses should still be tolerable so that stronger currents or longer pulses are possible. Thereby, one enters the regime of ultra-high dose rates, known as FLASH, where a magnetic field based range verification may become a more interesting approach, as its signal strength scales with the current and thus dose rate. In fact, considering the average rather than instantaneous
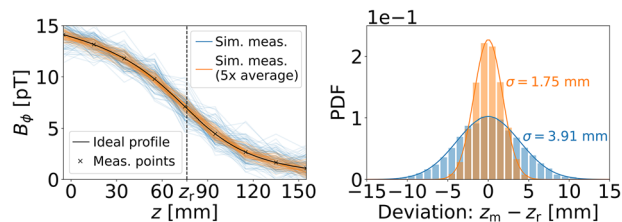
FIGURE 19 Theoretical accuracy of a range measurement. The simulated measurements are on the left, whereas the difference between measured (z_m) and actual range (z_r) is on the right. The latter is fitted with a normal distribution.

current, 0.2 µA is close to the necessary dose rate for FLASH[31].

Since the signal strength decreases with the distance from the source, it is preferable to place detectors as close as possible to the proton beam. Also, the longitudinal B-field profile flattens with increasing ρ (see Equation (18)), which provides further motivation to minimize the distance. How close sensitive magnetometry devices can be placed to the human body is also of interest in magnetoencephalography (MEG). SQUID detectors are as close as 2 cm away from the scalp[51], while using optical magnetometers a separation as low as 5 mm is possible[52,53]. In order to detect the B-field profile, one would need an array of detectors. Once again, we can take rough estimates from MEG, where a spacing of about 20–30 mm is used[54]. This may be sufficient considering the rather smooth profile from Figure 17.

Related to MEG, coping with noise from bioelectricity is a major concern toward a clinical application, as it potentially masks the sought signal. One potential approach to overcome this issue is by realizing that electromagnetic biological fields are in the low-frequency regime, reaching up to 100 Hz as known from MEG[54]. One may separate the low-frequency background from the signal of the proton beam by oscillating the beam current at frequencies above the biological threshold. As magnetometry can be tailored toward oscillating fields[55], it could enable a detection in the presence of noise by searching for the known reference frequency.

A detection would require shielding from external magnetic fields, which is common practice in MEG. Without active pencil beam scanning, the fringe fields in the treatment room are below mT, where the closest quadrupole magnet is 2.99 m away from the isocenter[56]. This should be even lower with the setup from Paul et al.[57], where the magnets are more than 6 m away from the isocenter.

Finally, based on the assumptions made in this section, we make an estimate regarding the accuracy of a potential range verification through a magnetic field measurement. Therefore, we have simulated a measurement process (see Figure 19) by randomly sampling the ideal magnetic field (B_ϕ-profile from Figure 17) at a few selected detector locations (longitudinally spaced by 20 mm over a distance of 16 and 5 cm away from the central beam axis) from a normal distribution. Strength and uncertainty are given above. We then fit the expected profile to the "measured data" and extract the longitudinal position. As shown in Figure 19, the accuracy of a single pulse measurement (0.1 Gy) would be about 3.91 mm, while an average over five pulses increases the accuracy to 1.75 mm.

4.8 | Limitations

The present study sought to establish a fundamental understanding regarding the impact of secondaries on the primary proton beam current and its associated magnetic field. A couple of simplifying assumptions were made, whose justifications and shortcomings are discussed here.

First, the uniform axial-symmetric geometry is only a very rough approximation of a patient-like target. Future work should consider more realistic phantoms. On the other hand, it enabled a reduction to two-dimensional or one-dimensional profiles and thereby a simple analysis. At the present early stage of these investigations, simplified geometries are crucial to extract general statements from complex simulated data. Also, within this study we compare the results to our previous analytical work, which was based on the same geometry.

Furthermore, this work relies on MC, which cannot simulate interactions between particles and therefore neglects conductive processes. For heterogeneous targets, small additional magnetic fields could arise from non-symmetric conduction currents. This needs to be simulated with a completely different numerical approach, far beyond this first assessment. Experimentally, impact of the target's conductivity could be assessed by a comparison with a non-conductive target, such as PMMA.

5 | CONCLUSION

Through the present work, we provided a comprehensive analysis of the static magnetic field created by a therapeutic proton beam. Initially, the necessity for a quasi-static FEA formalism, allowing for $\nabla \cdot \mathbf{J} \neq 0$ has been underlined and discussed. We also largely simplified the computational cost by exploiting the cylindrical symmetry and making use of exponential spacing. Relying on Geant4-DNA simulations, we find that the secondary electrons, despite their relative abundance, decrease the proton current by only about 10%, which is primarily caused by few directional head-on proton–electron collisions, while the vast majority (more than 98%) flows isotropically. The radial scattering leads to strongly fluctuating radial current, which can however be

neglected as it is two orders of magnitude below the longitudinal current. The accumulation laws show that the magnetic field from both lateral and longitudinal current is independent of the spot size. The increasing proton charge density along the beam explains the approximately constant current density, which is somewhat lowered by nuclear reaction losses. The latter, together with the electron current, shift back the magnetic field profile by approximately 2.4 mm at $\rho = 50$ mm. For $\rho > 45$ mm, the shift increases linearly. The relatively low proton count, despite a beam current of 0.2 μA, leads to strong fluctuations close to the beam, yet 10 cm away from the beam axis, the RSD drops below 2%. We also have argued that these fluctuations should have a negligible impact on a measurement. Finally we have discussed how a potential clinical application could be implemented.

Future work should lift the quasi-static assumption and further investigate the time dependence, including conductivity effects. Also, the precision of the suggested range verification needs to be further assessed. It depends on several factors such as geometry and target site, beam current, detector type and their accuracy (SQUID vs. optical magnetometry), detector placement, averaging, frequency dependence, and regression-based determination comparing expected vs. predicted profile. This should be feasible with the more fundamental analysis presented in this work. Whether the advantages (simple principle idea, signal strength scaling with the current) outweigh the challenges (experimental realization) need to be analyzed.

ACKNOWLEDGMENTS

CONFLICT OF INTEREST

The authors declare that there is no conflict of interest that could be perceived as prejudicing the impartiality of the research reported.

DATA AVAILABILITY STATEMENT

No data to share.

ORCID

Martin Rädler
https://orcid.org/0000-0003-3313-2993
Giulia Buizza
https://orcid.org/0000-0001-5504-1262
Maria Kawula
https://orcid.org/0000-0002-5039-8278
Guido Baroni
https://orcid.org/0000-0002-5464-0164
Chiara Paganelli
https://orcid.org/0000-0003-4787-8649
Katia Parodi https://orcid.org/0000-0001-7779-6690
Marco Riboldi
https://orcid.org/0000-0002-2431-4966

REFERENCES

1. Paganetti H. Range uncertainties in proton therapy and the role of Monte Carlo simulations. *Phys Med Biol*. 2012;57(11):R99.
2. Knopf A-C, Lomax A. In vivo proton range verification: a review. *Phys Med Biol*. 2013;58(15):R131.
3. Parodi K. Latest developments in in-vivo imaging for proton therapy. *Br J Radiol*. 2020;93(1107):20190787.
4. Krimmer J, Dauvergne D, Létang J, Testa É. Prompt-gamma monitoring in hadrontherapy: a review. *Nucl Instrum Methods Phys Res. A*. 2018;878:58–73.
5. Lascaud J, Dash P, Wieser H-P, Kalunga R, Wuerl M, Assmann W, Parodi K. Investigating the accuracy of co-registered ionoacoustic and ultrasound images in pulsed proton beams. *Phys Med Biol*. (2021);66(18):185007.
6. Albert J, Labarbe R, Sterpin E. Electric field from a proton beam in biological tissues for proton radiotherapy. *Phys Rev Appl*. 2018;10(4):044054.
7. Rädler M, Gianoli C, Palaniappan P, Parodi K, Riboldi M. Electromagnetic signal of a proton beam in biological tissues for a potential range-verification approach in proton therapy. *Phys Rev Appl*. 2021;15(2):024066.
8. Cirrone G, Amato N, Catalano R, et al. On the possibility to use the charge imbalance in patients undergoing radiotherapy: a new online, in vivo, noninvasive dose monitoring system. *Appl Sci*. 2021;11(15):7005.
9. Jin J-M. *Theory and Computation of Electromagnetic Fields*. John Wiley & Sons; 2011.
10. Rylander T, Ingelström P, Bondeson A. *Computational Electromagnetics. Texts in Applied Mathematics*. Springer; 2012.
11. Wang Q. *Practical Design of Magnetostatic Structure Using Numerical Simulation*. John Wiley & Sons; 2013.
12. Rädler M, Dedes G, Parodi K, Riboldi M. Exploring a novel concept for direct proton beam measurement via its magnetic field. AAPM 61st Annual Meeting, 2019.
13. Kleeven W. Accelerators for industrial and medical applications: the Superconducting Synchrocyclotron Project S2C2 (Part IV) in European Scientific Institute (Archamps): Joint Universities Accelerator School (JUAS); 2014.
14. Jin J-M. *The Finite Element Method in Electromagnetics*. John Wiley & Sons; 2015.
15. Jackson JD. *Classical electrodynamics*. John Wiley & Sons; 1999.
16. Demerdash N, Nehl T, Fouad F. Finite element formulation and analysis of three dimensional magnetic field problems. *IEEE Trans Magn*. 1980;16(5):1092–1094.
17. Plonus MA. *Applied Electromagnetics*. McGraw-Hill; 1978.
18. Bíró O, Preis K. On the use of the magnetic vector potential in the finite-element analysis of three-dimensional Eddy currents. *IEEE Trans Magn*. 1989;25(4):3145–3159.
19. Schenck JF. The role of magnetic susceptibility in magnetic resonance imaging: MRI magnetic compatibility of the first and second kinds. *Med Phys*. 1996;23(6):815–850.
20. Agostinelli S, Allison J, Amako K, et al. Geant4'a simulation toolkit. *Nucl Instrum Methods Phys ResA*. 2003;506(3):250–303.
21. Allison J, Amako K, Apostolakis J, et al. Geant4 developments and applications. *IEEE Trans Nucl Sci*. 2006;53(1):270–278.
22. Allison J, Amako K, Apostolakis J, et al. Recent developments in Geant4. *Nucl Instrum Methods Phys Res A*. 2016;835:186–225.
23. Bernal M, Bordage MC, Brown JMC, et al. Track structure modeling in liquid water: a review of the Geant4-DNA very low energy extension of the Geant4 Monte Carlo simulation toolkit. *Phys Medica*. 2015;31(8):861–874.

24. Incerti S, Kyriakou I, Bernal MA, et al. Geant4-DNA example applications for track structure simulations in liquid water: a report from the Geant4-DNA Project. *Med Phys*. 2018;45(8):e722–e739.

25. Incerti S, Ivanchenko A, Karamitros M, et al. Comparison of Geant4 very low energy cross-section models with experimental data in water. *Med Phys*. 2010;37(9):4692–4708.

26. Incerti S, Baldacchino G, Bernal M, et al. The Geant4-DNA project. *Int J Model Simul Sci Comput*. 2010;1(02):157–178.

27. Derenchuk V. Particle beam technology and delivery: cyclotrons. 55th Annual AAPM Meeting: Proton Symposium, 2013.

28. Farr J, Mascia A, Hsi W-C, et al. Clinical characterization of a proton beam continuous uniform scanning system with dose layer stacking. *Med Phys*. 2008;35(11):4945–4954.

29. Pearson E, Kleeven W, Van de Walle J, Zaremba S. The new IBA superconducting synchrocyclotron (S2C2): from modelling to reality. Eleventh International Topical Meeting or Nuclear Applications of Accelerators; 2013.

30. Seidel M. *Cyclotrons*. The CERN Accelerator School 2018.

31. Jolly S, Owen H, Schippers M, Welsch C. Technical challenges for FLASH proton therapy. *Physica Med*. 2020;78:71–82.

32. van de Walle J, Abs M, Conjat M, et al. The S2C2: from source to extraction. Proceedings of the 21st International Conference on Cyclotrons and their Applications; ETH & PSI 2016:285–289.

33. Henrotin S, Abs M, Forton E, et al. Commissioning and testing of the first IBA S2C2. Proceedings of the 21st International Conference on Cyclotrons and their Applications; ETH & PSI 2016:178–180.

34. Moteabbed M, Yock TI, Depauw N, Madden TM, Kooy HM, Paganetti H. Impact of spot size and beam-shaping devices on the treatment plan quality for pencil beam scanning proton therapy. *Int J Radiat Oncol Biol Phys*. 2016;95(1):190–198.

35. Paganetti H. *Proton Therapy Physics*. CRC Press; 2018.

36. Bohr N. LX. On the decrease of velocity of swiftly moving electrified particles in passing through matter. *Philos Mag J Sci*. 1915;30(178):581–612.

37. Berger M, Coursey J, Zucker M, Chang J. ESTAR, PSTAR, ASTAR: computer programs for calculating stopping-power and range tables for electrons, protons, helium ions. National Institute of Standards and Technology (NIST), Gaithersburg, MD. Accessed April 9, 2019. 2005. http://physics.nist.gov/Star

38. de Vera P, Abril I, Garcia-Molina R. Energy spectra of protons and generated secondary electrons around the Bragg peak in materials of interest in proton therapy. *Radiat Res*. 2018;190(3):282–297.

39. de Vera P, Surdutovich E, Abril I, Garcia-Molina R, Solov'yov AV. Analytical model of ionization and energy deposition by proton beams in subcellular compartments. *Eur Phys J D*. 2014;68(4):1–8.

40. Kia MR, Noshad H. Comparison of the secondary electrons produced by proton and electron beams in water. *Phys Plasma*. 2016;23(5):053120.

41. Villagrasa C, Francis Z, Incerti S. Physical models implemented in the GEANT4-DNA extension of the GEANT-4 toolkit for calculating initial radiation damage at the molecular level. *Radiat Prot Dosim*. 2011;143(2–4):214-218.

42. Kyriakou I, Šefl M, Nourry V, Incerti S. The impact of new Geant4-DNA cross-section models on electron track structure simulations in liquid water. *J Appl Phys*. 2016;119(19):194902.

43. Rohatgi V, Saleh A, (Firm) P. *An Introduction to Probability Theory and Mathematical Statistics*. Wiley Series in Probability and Statistics. John Wiley & Sons, Incorporated; 2015. Corollary following Theorem 3 on p. 135 in Section *4.4: Functions of several random variables*.

44. Podgoršak E. *Biological and Medical Physics, Biomedical Engineering. Radiation Physics for Medical Physicists*. Springer; 2010.

45. Rudd ME Kim, Y-K, Madison DH, Gay TJ. Electron production in proton collisions with atoms and molecules: energy distributions. *Rev Mod Phys*. 1992;64(2):441.

46. Emfietzoglou D, Papamichael G, Kostarelos K, Moscovitch M. A Monte Carlo track structure code for electrons (10 eV–10 keV) and protons (0.3–10 MeV) in water: partitioning of energy and collision events. *Phys Med Biol*. 2000;45(11):3171.

47. Francis Z, Incerti S, Capra R, et al. Molecular scale track structure simulations in liquid water using the Geant4-DNA Monte-Carlo processes. *Appl Radiat Isot*. 2011;69(1):220–226.

48. Pizzochero M, Ambrosio F, Pasquarello A. Picture of the wet electron: a localized transient state in liquid water. *Chem Sci*. 2019;10(31):7442–7448.

49. Drung D, Abmann C, Beyer J, et al. Highly sensitive and easy-to-use SQUID sensors. *IEEE Trans Appl Supercond*. 2007;17(2):699–704.

50. Lehrack S, Assmann W, Bertrand D, et al. Submillimeter ionoacoustic range determination for protons in water at a clinical synchrocyclotron. *Phys Med Biol*. 2017;62(17):L20.

51. Coquelet N, De Tiège X, Destoky F, et al. Comparing MEG and high-density EEG for intrinsic functional connectivity mapping. *NeuroImage*. 2020;210:116556.

52. Iivanainen J, Stenroos M, Parkkonen L. Measuring MEG closer to the brain: Performance of on-scalp sensor arrays. *NeuroImage*. 2017;147:542–553.

53. Hill RM, Boto E, Rea M, et al. Multi-channel whole-head OPM-MEG: helmet design and a comparison with a conventional system. *NeuroImage*. 2020;219:116995.

54. Hämäläinen M, Hari R, Ilmoniemi RJ, Knuutila J, Lounasmaa OV. Magnetoencephalography' theory, instrumentation, and applications to noninvasive studies of the working human brain. *Rev Mod Phys*. 1993;65(2):413.

55. Savukov IM, Seltzer S, Romalis M, Sauer K. Tunable atomic magnetometer for detection of radio-frequency magnetic fields. *Phys Rev Lett*. 2005;95(6):063004.

56. Gantz S, Hietschold V, Hoffmann AL. Characterization of magnetic interference and image artefacts during simultaneous in-beam MR imaging and proton pencil beam scanning. *Phys Med Biol*. 2020;65(21):215014.

57. Paul K, Dorsch S, Naumann J, et al. *Towards MR-guided particle radiotherapy: compatibility of an open MR scanner with an ion beamline*. Radiotherapy & Oncology 170, ESTRO; 2022.

SUPPORTING INFORMATION

Additional supporting information can be found online in the Supporting Information section at the end of this article.